RELIABLE ACOUSTIC LINK USING NON-COHERENT TURBO-CODED FSK

by

Andrew Alexander Dobbin

Submitted in partial fulfillment of the requirements
for the degree of Master of Applied Science

at

Dalhousie University
Halifax, Nova Scotia
April 2018

Table of Contents

List of Tables

List of Figures

Abstract

The contents of this thesis explore the challenge of implementing a reliable, wireless, communication link in the highly variable environments of shallow underwater channels. The physical variability of the underwater acoustic channel is described with respect to signal attenuation, acoustic wave reflection and refraction, and temporal variation due to motion. These characteristics are implemented in a software model to represent a realistic ocean environment for in-lab algorithm design. The process for designing simple, non-coherent communication algorithms (32-FSK and 16-parallel BFSK) to achieve robust performances are discussed. Robustness is achieved through the implementation of turbo code.

The results of the communication algorithms demonstrate successful communication for distances up to 10 km validated through sea trial, but yielded low-data rates (32 bps to 1.67 bps). Zero errors were received during the sea trial for the turbo coded algorithms. To confidently quantify the reliability of these algorithms, more symbols must be transmitted.

List of Abbreviations and Symbols Used

$\alpha(f)$	Frequency dependent absorption coefficent
a, a_p	Attenuation, path dependent attenuation
α	Past state probability
A	Amplitude
AC	Alternating Current
ADB	Application Data Block
ADC	Analog to Digital Converter
ADCP	Acoustic Doppler Current Profiler
AIS	Automatic Identification System
AUV	Autonomous Underwater Vehicle
AWGN	Additive White Gaussian Noise
β	Future state probability
bps	Bits per second
B_{coh}	Coherence bandwidth
B_{n-n}	Null to null bandwidth
Bd	Baud rate
BCJR	Bahl, Cocke, Jelinek and Raviv
BER	Bit Error Rate
BFSK	Binary FSK

c_w	Speed of sound underwater
CIR	Channel Impulse Response
CTD	Conductivity, Temperature,and Depth
dB	Decibels
D_s	Doppler spread
DAC	Digital to Analog Converter
DC	Direct Current
DFO	Department of Fisheries and Oceans
DRDC	Defence Research and Development Canada
DSSS	Direct Sequence Spread Spectrum
E_b	Energy per bit
f_c	Carrier frequency
$f_d(t)$	Time dependent Doppler shift
Δf	Frequency separation
Δf_{min}	Minimum frequency separation
FEC	Forward Error Correction
FHSS	Frequency Hopping Spread Spectrum
FSK	Frequency Shift Keying
γ	Present state probability
G	Conductance
GPS	Global Positioning System

$h(t, \tau)$	Time dependent and delay dependent CIR
$h(\tau)$	Delay dependent channel impulse response
Hz	Hertz
ICI	Inter-Carrier Interference
ISI	Inter-Symbol Interference
k	Bits per symbol
km	Kilometer
λ	Wavelength
L	Number of hopping bands
LFM	Linear Frequency Modulation
LLR	Log Likelihood Ratio
LPF	Low Pass Filter
LTI	Linear Time Invariant
M	Modulation order
MAP	Maximum A Posteriori
MFSK	Multiple Frequency Shift Keying
MIMO	Multiple Input Multiple Output
MP	Multipath
N	Spreading factor
N_p	Number of paths
N_0	Noise spectral density

NATO	North Atlantic Treaty Organization
OFDM	Orthogonal Frequency Division Multiplexing
P	Number of parallel transmissions
P_{be}	Probability of bit error
P_{AP}	Probability a priori
PA	Power Amplifier
PSD	Power Spectral Density
PSK	Phase Shift Keying
r	distance between transmitter and receiver
r_o	length of half the water column
$r(t)$	Received signal
R_b	Bit rate
R_s	Symbol Rate
RF	Radio Frequency
RMS	Root Mean Square
RSC	Recursive Systematic Convolutional
σ_t	RMS Multipath Delay Spread
$s(t)$	Transmitted signal
S	Hydrophone sensitivity
SL	Signal Level
SNR	Signal to Noise Ratio

SPL	Sound Pressure Level
SSP	Sound Speed Profile
Θ_p	Path dependent incident angle
τ, τ_p	Time delay, path dependent time delay
T, T_s	Symbol period
T_c	Chip period
TL	Transmission Loss
TR	Turbulent Research
TVR	Transmit Voltage Response
$\mu(t)$	Time dependent Doppler scaling ratio
UPS	Uninterruptible Power Supply
USB	Universal Serial Bus
UUV	Unmanned Underwater Vehicle
$v_r(t)$	Time dependent relative velocity
VLA	Vertical Line Array
w	Wind speed, m/s
W	Total bandwidth
W_L	Hopping bandwidth
Y	Admittance

Acknowledgements

I would like to express my sincere appreciation and gratitude to my supervisor, Dr. Jean-François Bousquet, for his invaluable guidance, patience, and expertise throughout the writing of this thesis. His support throughout my Master's degree program has been an enriching experience personally, professionally, and academically.

To my committee members, Dr. Paul Hines and Dr. David Barclay, a most sincere and appreciative thank you for all of your assistance over the last year. I am grateful for you dedicating time from your hectic schedules to review and enrich my work.

I would like to thank my colleagues of the UW-STREAM research lab, managed by Dr. Bousquet, for providing a friendly and co-operative research environment. It has been a pleasure meeting, bonding, and learning from every one of you.

I am indebted to General Dynamics Mission Systems Canada and to the Mitacs Accelerate Program for providing me the opportunity to pursue a highly technical industry-supported project and to the government of Nova Scotia by providing research funding through the Nova Scotia Graduate Scholarship.

Finally, I would extend my love and appreciation for the support of my parents, my family, my friends, and my girlfriend for continually motivating me. The love you gave and continue to give is the source of my inspiration. This work would not have been possible without your support, and encouragement.

Chapter 1

Introduction

1.1 Background

Acoustic propagation is widely considered the best method for underwater communication and is particularly attractive for long range transmission. Other methods for communicating have been attempted, such as optical, magnetic induction, and electromagnetic. Each of these methods offer their own advantages and disadvantages, such that the specific application must be considered when choosing the most appropriate mode. Optical communication can provide extremely high speed data rates but requires *line of sight* between the transmitter and receiver, which limits the range of the communication link to a few hundred meters [1]. Note that optical systems see a reduction in performance due to interference from sunlight and turbidity. Magneto-inductive and electromagnetic methods can both produce very high rate systems but are range limited from several 10s to 100s of meters, due to the high electrical conductivity of sea water [1]. Alternatively, *long range* underwater wireless communication is dominated by the use of acoustic sound waves, with range capabilities on the order of 10s to 100s of kilometers but are limited to comparatively slow data rates. For long range, reliable communication, acoustics is the most promising solution and will be the focus of this work.

The aim of this project is to implement and test in realistic conditions, a long range communication link that provides robustness against harsh acoustic ocean environments up to 10 km. The communication link is intended to transmit short bursts of data incorporating a small alphabet to relay simple messages to the receiver. This can enable monitoring of the subsea environment using remote platforms. For example, for a fully submerged vehicle the only way to relay information at long range is with an acoustic point-to-point link. This low data rate, long range link provides

the submerged vehicle with communication capabilities and information regarding its acoustic network. These type of acoustic networks are typically employed for military surveillance purposes where acoustic network monitoring is essential.

Other potential applications include underwater sensor networks for commercial, scientific, and environmental purposes. The use of long distance communication may be applied to networks of autonomous underwater vehicles (AUVs) and unmanned underwater vehicles (UUVs) to enable exploration of remote subsea environments [2]. Fixed subsea networks may also be used to track marine pollutants, study seismic activity, assist in navigation, and collect oceanographic data.

1.2 Objectives

In this thesis, the design of an underwater acoustic communication link physical layer will be developed and tested in realistic conditions. Focusing on simple implementation and signal processing, a robust link capable of achieving long range communication at the expense of data throughput is the main objective. The main functional requirements of the communication link are:

- Robust signaling in adverse underwater acoustic environments subject to multipath and time-variance,
- Low complexity implementation and signal processing algorithms,
- Capability of long range communication up to 10 km,
- Using a narrowband projector at a center frequency of 2 kHz, achieve a reliability better than 10^{-3} for a low throughput on the order of 10 bps.

To achieve the objectives in this project, a rigorous scientific research methodology is applied. Specifically, this methodology includes channel modeling, simulations, and validation in realistic conditions at sea. First, the background physical propagation of acoustic waves underwater is reviewed. Further, analytical models are utilized to replicate channel impairments. The models are then included in the simulation of the communication algorithms, such that the validity of theoretical models in controlled

conditions is confirmed. To confirm the simulation results, a sea trial in realistic conditions serves to confirm the performance of the link. The results from the sea trial are used to compare compatibility and performance with current state of the art technologies.

In this research modern oceanographic modeling techniques are used to simulate the performance of communication algorithms in realistic ocean conditions. Also in this research, the design of a low-complexity multi-carrier modulation algorithm to combat the harshness of the underwater channel. Spread spectrum techniques, the implementation of a high performance forward error correction technique, and their effectiveness at increasing signal reception reliability was also studied. The performance of the system is validated through a thorough and intense sea trial to confirm the simulation results.

1.3 Thesis Outline

The remainder of this thesis is organized as follows. Chapter 2 discusses the physical phenomenon that affect underwater acoustic signals and systems. Chapter 3 discusses the process for designing a reliable non-coherent communication link to serve the purposes outlined above. Chapter 4 discusses the procedure for physical ocean experimentation, including hardware setup and calibration, sea-trial schedule, and post-processed results. Chapter 5 concludes the thesis, reiterating contributions, and provides insight on the future direction of this research.

Chapter 2

Underwater Acoustic Propagation

Underwater acoustic propagation is predominately affected by the sound speed profile of the water column, transmission losses due to signal spreading and absorption, multipath reflections on ocean boundaries, and temporal variations of the ocean due to motion. The large-scale properties of an acoustic channel are modeled using an acoustic propagation model, such as the Bellhop model.

The objective of this Chapter is to provide a high level overview of the physical properties of acoustic propagation. In Section 2.1, the transmission loss of an acoustic wave is described with respect to spherical and cylindrical spreading. Section 2.2 describes the sound speed profile of the water column, its dependencies on pressure, temperature, and salinity, and how the speed of sound affects acoustic communication. Section 2.3 describes the phenomenon of multipath arrivals due to boundary reflections, and refraction. Section 2.4 discusses temporal variations such as Doppler shift and spread due to relative motion of platforms and the environment. Lastly, Section 2.5 describes the Bellhop model, used to recreate models of the described underwater acoustic propagation characteristics.

2.1 Transmission loss

This section describes and quantifies the transmission loss of an acoustic wave due to signal spreading, the effect of frequency absorption and how it relates to attenuation.

If the acoustic signal is being transmitted from a point source then the acoustic wave propagates radially away from the source. The signal intensity attenuates following an inverse square law, known as spherical spreading. However, in shallow water environments spherical spreading cannot be maintained. If the distance from

the source to the receiver is greater than the distance from the source to the channel's boundaries, then the wave spreads in a cylindrical fashion. For the distance from the source to the receiver defined as r, the transmission loss due to spherical spreading can be calculated as 20 times the log of r. Spherical spreading is valid when the receiver's distance is less than half of the water column, r_o [3]. Beyond the range r_o, the loss is approximated to follow cylindrical spreading. The transmission loss is calculated as 10 times the log of the difference between r and r_o. Therefore, the total loss due to spreading, TL_{Spread}, can be calculated as:

$$TL_{spread} = \begin{cases} 20\log(r) & \text{if } r < r_o, \\ 20\log(r) + 10\log(r - r_o) & \text{if } r > r_o. \end{cases} \tag{2.1}$$

Transmission loss is also observed as a function of frequency. Specifically, as the frequency increases, the acoustic energy gets absorbed and the energy is converted into heat [3]. The absorption loss, $\alpha(f)$ $[dB/km]$, depends on properties of the sea water, and an empirical model as a function of frequency is demonstrated in [3]. Combining the absorption loss with spreading loss then the total transmission loss of an acoustic signal can be approximated by:

$$TL_{Total} = \begin{cases} 20\log(r) + \alpha(f)\frac{r}{1000} & \text{if } r < r_o, \\ 20\log(r) + 10\log(r - r_o) + \alpha(f)\frac{r}{1000} & \text{if } r > r_o. \end{cases} \tag{2.2}$$

This equation assumes no losses due to boundary interactions and reflections. The combined effect of absorption and spreading loss can be seen in Figure 2.1 as a function of distance for different frequencies. Figure 2.1 shows the transmission loss of an acoustic wave in dB versus distance to receiver for varying frequencies. As the frequency increases, the loss per kilometer drastically increases. As such, it can be observed that to achieve high data rates in a communication system with a high center frequency, the transmitter and receiver need to be in close proximity. Low frequency systems which support slower data rates can achieve greater distances before the signal is greatly attenuated. Although lower frequency signals attenuate less than higher frequency signals, the difference is offset due to higher ambient noise at lower frequencies. This is primarily due to shipping activity and surface roughness [4].

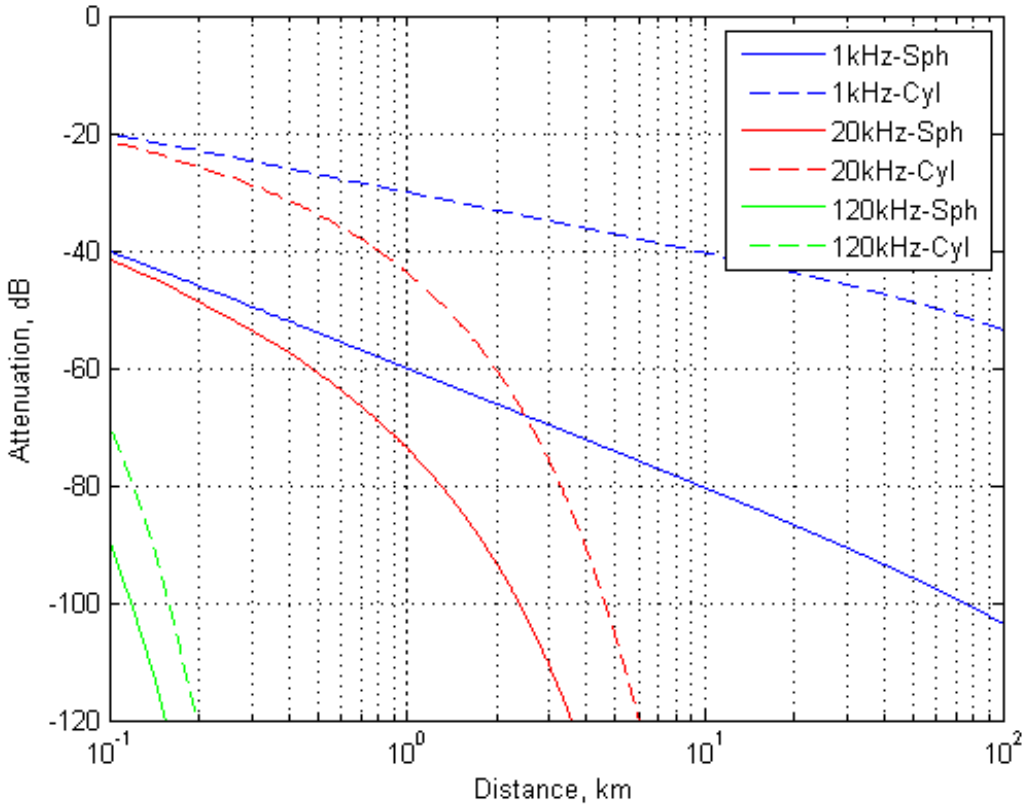

Figure 2.1: Transmission loss

2.2 Sound Speed Profile

In this section, the effect of the low propagation speed, and its variable sound speed profile (SSP) is introduced and discussed with regards to its relevance to communication systems, specifically with respect to bandwidth limitations, latency, and inter-symbol interference.

The underwater speed of sound is on the order of 1500 m/s. This is several orders magnitude lower than the speed of light in RF communication systems. The slow propagation drastically increases the latency between the transmitter and receiver and severely limits the available bandwidth in acoustic systems. Having a large propagation delay also causes reflected echoes from a previously transmitted symbol to corrupt subsequent symbols. This results in inter-symbol interference (ISI). The propagation delay, τ, is dependent upon the speed of sound of the acoustic wave, c_w, and the distance, d, of the path taken, such that $\tau = d/c_w$. However, the speed of

sound is not a constant value in the ocean; it depends on the temperature, pressure, and salinity of water. The SSP represents the speed of sound at varying depths along the water column. The variance of the sound speed with depth is significant because it causes refraction or ray-bending of the acoustic signal towards the lower speed. Figure 2.2 represents multiple SSPs taken by an ocean gilder in May 2011 that is similar to the environment of the July 2017 sea trial. It illustrates the speed variability that may be noticed, however, water mass, location, and season all affect a specific water columns SSP.

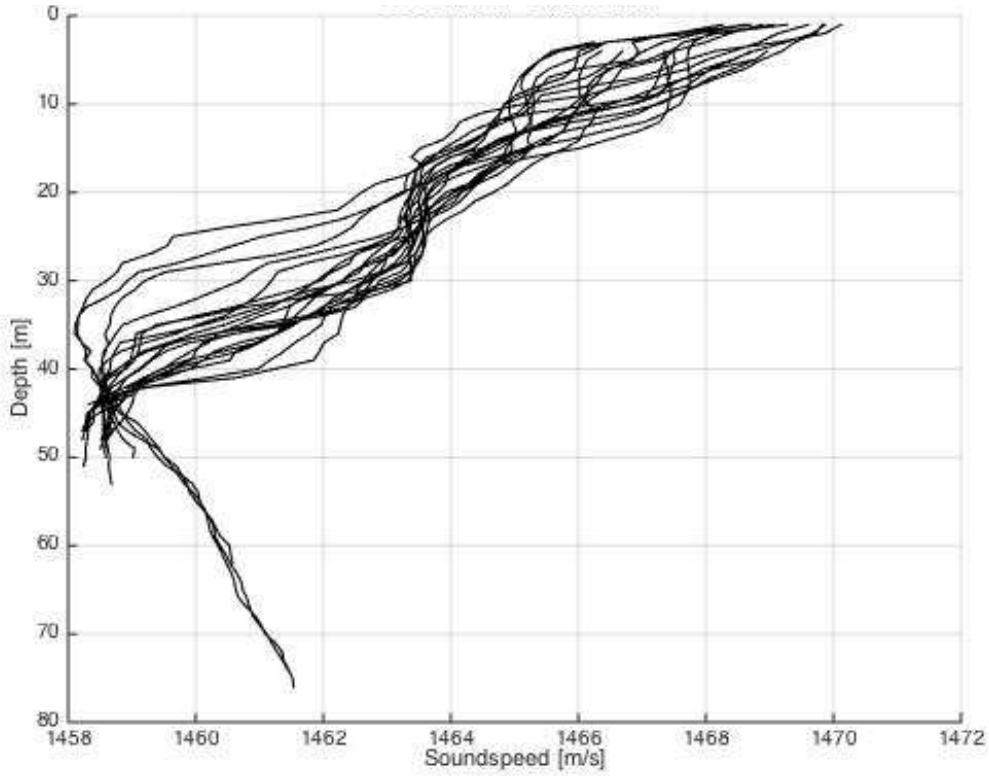

Figure 2.2: Multiple ocean gilder SSPs for 80 m deep water column

As can be seen, the speed of sound fluctuates significantly. The sound speed minimum of the SSP, located at approximately 43 m deep as shown in the figure, represents an ideal location for the deployment of an acoustic transmitter since at this height a form acoustic waveguide is found. The sound waves, when propagating upwards will tend to bend downwards, and a wave propagating downwards will bend upwards. Since the SSP of the water column is highly dependent on pressure (depth), temperature, and salinity, it varies drastically with the environment. The

most accepted expression for the speed of sound in water was derived by Wilson [5]. However, as this equation was too computationally extensive, Leroy [6] simplified the formula shown as:

$$c = 1492.9 + 3(T-10) - 6\times10^{-3}(T-10)^2 - 4\times10^{-2}(T-18)^2 + 1.2(S-35) - 10^{-2}(T-18)(S-35) + Z/61. \quad (2.3)$$

In this expression only, T is the temperature in degrees centigrade, S is the salinity in parts per thousand, and Z is the depth in meters. For example, coastal waters typically are very shallow and the isothermal layer may be relatively large compared to the water depth. These environments' temperatures may change significantly with the season, warming water temperatures during the summer, and will greatly affect the SSP. With a highly variable environment, the SSP will have to be measured before transmitter deployment to optimize signal reception.

2.3 Multipath

The concept of multipath arrivals and its affect on the underwater communication systems is introduced in this section. A mathematical representation of the multipath communication channel is described.

When a transmitted signal interacts with a boundary, such as the surface or sea floor, a reflection occurs with a departure angle found according to Snell's Law. The departure angle and signal strength of bottom reflections depend upon the consistency and density of the material on the ocean floor. Figure 2.3 shows an example of a 4-path environment including the respective amplitude and distance for each path. The paths consist of an idealized direct path (path 0), a refracted direct path due to change in speed of sound with depth (path 1), a surface reflection (path 2), and a bottom reflection (path 3). These multiple refractions and reflections are delayed versions of the signal and interfere with the original signal. In addition, a varying

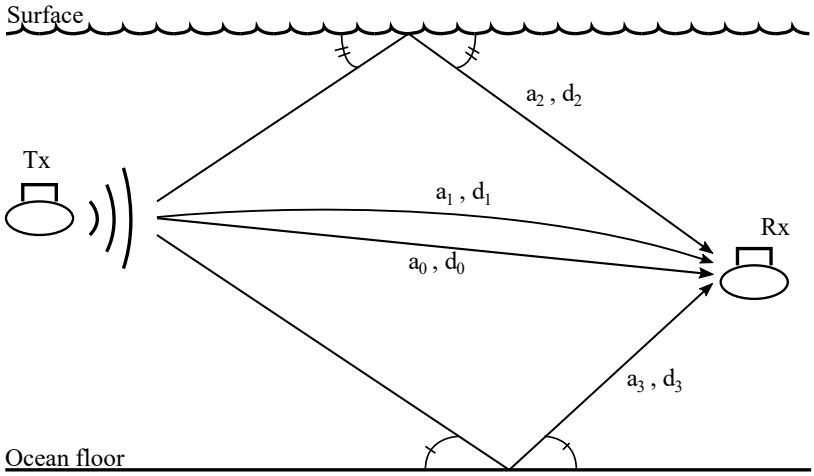

Figure 2.3: 4-discrete multipath arrivals

sound speed profile creates additional bends in the reflected arrivals causing an increasingly complex multipath profile. The discrete channel impulse response (CIR) of a multipath environment is described as the summation of a select number of discrete path arrivals, each arrival with a path dependent amplitude and time delay:

$$h(\tau) = \sum_{p=1}^{N_p} a_p \delta(\tau - \tau_p), \tag{2.4}$$

where N_p represents the number of paths, a_p is the individual path amplitude, and τ_p is each paths delay [7]. If one represents the channel as a linear time-invariant (LTI) system, the continuous-time received signal, $r(t)$, is obtained by convolving the transmitted signal $s(t)$ with the CIR, $h(t)$:

$$r(t) = \int_{-\infty}^{+\infty} h(\tau) s(t - \tau) d\tau \tag{2.5}$$

When discussing multipath an important parameter is the root-mean-square (RMS) delay spread, σ_t. The RMS delay spread is used to measure the richness of the multipath environment, often defined as the time between the first path arrival and the last significant path arrival, calculated by:

$$\sigma_t = \sqrt{\overline{\tau^2} - (\overline{\tau})^2}, \tag{2.6}$$

where,

$$\overline{\tau} = \frac{\sum_p a_p^2 \tau_p}{\sum_p a_p^2} \qquad \text{and} \qquad \overline{\tau^2} = \frac{\sum_p a_p^2 \tau_p^2}{\sum_p a_p^2}. \tag{2.7}$$

The resulting σ_t is the standard deviation of each paths delay weighted proportionally against its respective signal energy. It is an approximation of the multipath CIR richness and is useful for designing robust communication systems.

2.4 Temporal Variations

This section discusses the motion dependent nature of the underwater channel. Motion is described with respect to time variability in a non-static environment.

In the previous section the channel was approximated as a linear time-invariant (LTI) system. However, the underwater channel is not time-invariant as it does fluctuate with time. A couple of examples of time variance include platform mobility (causing Doppler) and ocean waves (causing scatter and time delay). The Doppler effect can be categorized into Doppler spread and Doppler shift. Doppler shift can be caused by the relative motion from one platform to the other and it can either increase or decrease the frequency of the acoustic signal. Additionally, the motion of the ocean environment can cause individual Doppler shifts on each independent path. Doppler spread occurs when multiple signals are receiver with different Doppler shifts. The difference between simultaneously received Doppler shifts is the Doppler spread.

Effectively, the change of location of the platform causes the multipath profile to continuously change, varying the amplitudes, phases, and delays associated with each path. The individual path amplitude variations due to relative motion of the platforms are typically negligible. However, significant amplitude variations occur by the changing combination of the multipath paths due to the change in time.

In a narrowband system, the compression or dilation of the frequency results in a Doppler frequency shift and is calculated using a time-varying scaling ratio, μ. The

scaling ratio is defined as the ratio between relative velocity of the platforms, v_r, with respect to the velocity of sound underwater, c_w. Assuming the frequency sent is at the carrier frequency, f_c, then the frequency Doppler shift, f_d, is calculated as the relative velocity divided by the speed of water multiplied by the carrier frequency:

$$f_d(t) = \frac{v_r(t)}{c_w} f_c = \mu(t) f_c. \tag{2.8}$$

Furthermore, since each path may be subject to a different Doppler shift. Doppler Spread, D_s, is the measure of difference between the largest Doppler shift, f_{di}, and the smallest Doppler shift [7], f_{dj}, shown in the equation below:

$$D_s = \max f_{di}(t) - f_{dj}(t). \tag{2.9}$$

Combining the frequency shift due to Doppler with a time-varying multipath profile results in:

$$h(t,\tau) = \sum_{p=1}^{N_p} a_p(t)\delta(\tau - \tau_p(t)) \exp(j2\pi(f_d(t,\tau))t). \tag{2.10}$$

This frequency offset also varies in time as the relative velocity between the platforms, the channel motion, and platform positions in the water column vary the Doppler scaling factor.

The amplitude variation is attributed to the changing multipath profile, however, when the acoustic wave is incident on objects with dimensions on the order of half wavelength, scattering occurs. Scattered rays vary in amplitude and their path may differ slightly from the original path. This causes additional multipath echoes with closely arriving path delays. A cluster is described as the reception of a group of scattered rays. The arrival of the clusters follows a similar multipath profile as described earlier with an added depth of complexity. This type of channel model was originally described for RF applications [8], but has been recently applied to model underwater acoustic propagation [9].

2.5 Ray Tracing Model

This section introduces the Bellhop model and its ability to generate representative power tracing profiles and CIR's for specific ocean environments.

The Bellhop model is a finite element simulation tool used to represent the acoustic channel in varying underwater environments. It accounts for spreading, absorption, and the variable velocity of sound to create a ray-tracing profile. It can also be used to simulate the propagation loss for each of the multipath arrivals. In this work, the purpose of the Bellhop model is to create the multipath profile for the arrival of clusters for a realistic underwater environment.

Figure 2.4 shows a Bellhop model run for a specific shallow water environment with an interpolated sound speed profile matched to Figure 2.2. The figure shows a highly concentrated ray-bending and reflective environment and highlights refraction around the sound speed minimum.

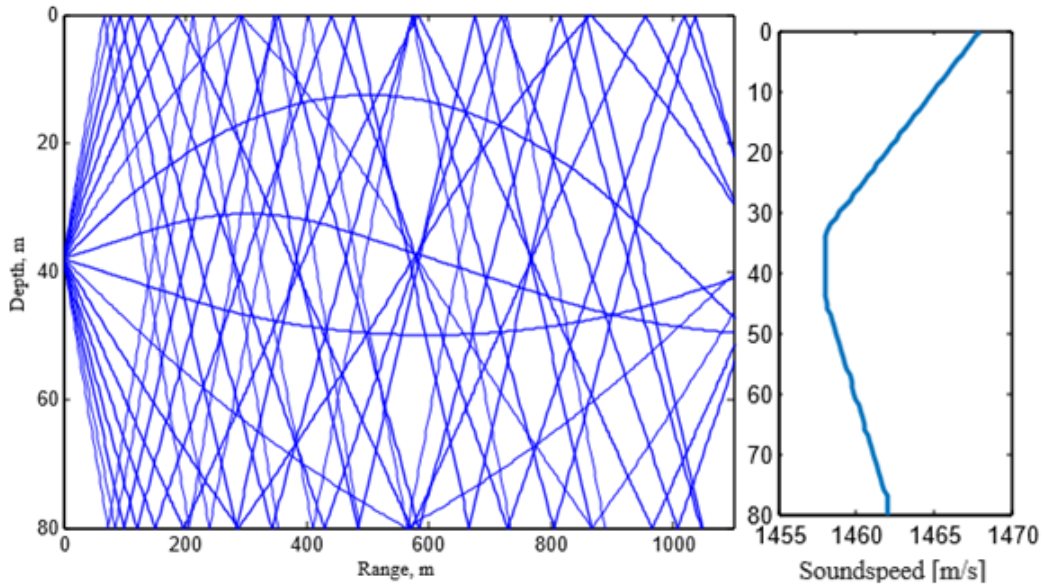

Figure 2.4: Bellhop Ray-tracing Multipath model

Shown in Figure 2.5 is the power profile associated with each ray traced by the Bellhop model for ranges up to 12 km. This figure is a visual representation of the transmission loss to be expected for the 10 km range of the sea trial.

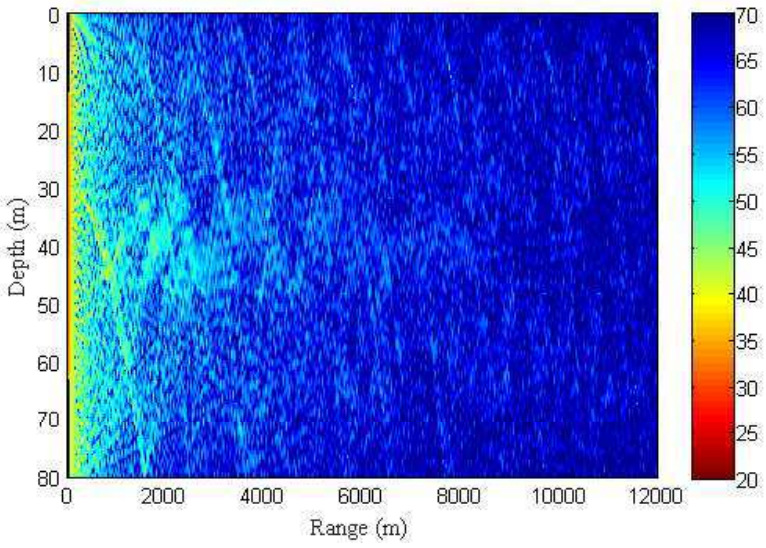

Figure 2.5: Bellhop Ray-tracing transmission loss model

To adequately estimate the value of the multipath delay spread, the Bellhop model is also used to generate a channel impulse response for a 10 km, 80 m deep underwater environment, as shown in Figure 2.6. This figure is bandlimited to the baseband bandwidth of 320 Hz, the approximate 3 dB bandwidth of the projector utilized during the sea trials. The propagation delay between transmitter and receiver is not included in this figure; time zero is relative to the start of signal reception. Extracted from the CIR, an estimate for the multipath delay spread is approximately 0.18 seconds, or the time when the CIR amplitude matches the background ambient noise.

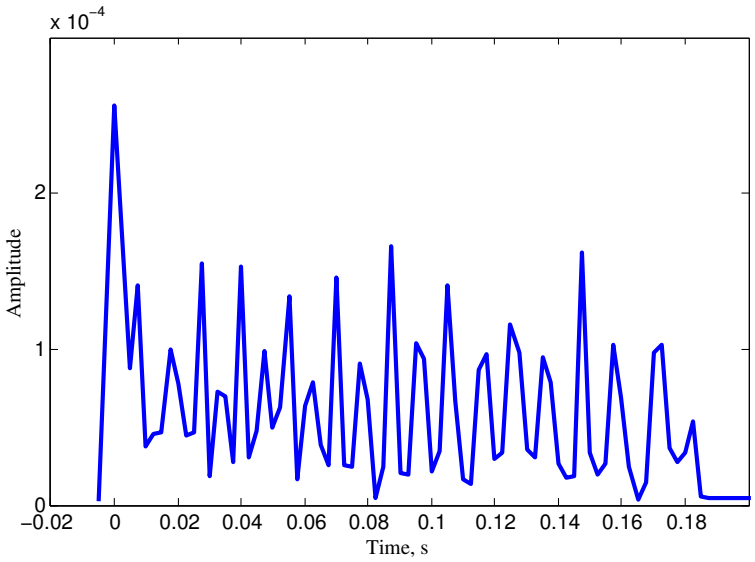

Figure 2.6: Bellhop Model: Discrete-Time Channel Impulse Response

Chapter 3

Non-Coherent Multi-Carrier Modulation

This chapter discusses the properties of non-coherent modulation techniques proposed for underwater communication. The concept of orthogonality and phase coherence will be discussed and applied to each of the proposed algorithms. Following the modulation design, signal spreading techniques will be discussed as methods to increase reliability of data reception. Each modulation technique will be simulated in MATLAB for variable channel conditions. Bit error rate (BER) is used to quantify robustness of each technique.

This chapter is outlined as follows: Section 3.1 discusses current state-of-the-art technologies using frequency shift keyed (FSK) modulation schemes for underwater communications. Section 3.2 introduces the concept of orthogonality in multi-carrier communication systems and defines the ideal frequency spacing between subcarriers. Section 3.3 describes the characteristics of non-coherent systems. Section 3.4.1 discusses the algorithm development for implementing a non-coherent, orthogonal, multiple frequency shift keying (M-FSK) modulation. Section 3.4.3 describes an alternate to M-FSK modulation, describing an adaptation by implementing a parallel-tone binary FSK (BFSK) modulation technique. Section 3.5 describes existing spread spectrum techniques to improve robustness in adverse environments, and also discusses the implementation of a forward error correction (FEC) code known as the turbo code. Lastly, in Section 3.6 describes the compatibility with the Janus NATO standard for digital underwater communications.

3.1 Current State-of-the-art

To assess the current state-of-the-art, an analysis of the evolution of non-coherent modulation techniques are shown in Table 3.1 [10]. Note, the d and s refer to *deep* and *shallow* waters, respectively.

Researcher	**Bandwidth**	**Range**	**Bit Rate**	**BER**
Catipovic '84 [11]	5 kHz	3_s km	1.2 kbps	10^{-2}
Freitag '91 [12]	5 kHz	2.9_d km	0.6 kbps	10^{-3}
Mackelburg '91 [13]	10 kHz	2_d km	1.25 kbps	N/A
Scussel '97 [14]	5 kHz	$10_d - 5_s$ km	0.6-2.4 kbps	N/A

Table 3.1: Evolution of non-coherent modulation techniques

Notably, in 2001 [15], a FH-FSK waveform is transmitted in a very shallow-water, highly frequency selective, channel using a center frequency of 13.5 kHz and a bandwidth of 4800 Hz. The performance of the various trials achieved a BER of 10^{-2} to 10^{-4} while the data throughput ranged from 320 bps to 19 bps, respectively.

More recently in 2016, a frequency hopping, time hopping, binary-orthogonal keying LFM modulation type utilizing a carrier frequency between 500 to 800 kHz designed for extremely short range communication [16]. A data rate of 110 bps is achieved in a 10 m distance, 6.5 m depth sea trial. The experiment transmitted 100,000 bits achieving zero errors with an average SNR of 19 dB.

During this year, 2018, Cao et al [17] performed a 1 km, 10 m deep, sea trial on an MFSK acoustic signal while utilizing time reversal techniques and channel encoders to reduce errors. The band utilized spread from 13 kHz to 18 kHz and employed a data rate of 293 bps. Table 3.2 lists the correcting techniques and BER results obtained during the sea trial performed by Cao et al [17].

Time Reversal	**Encoding**	**BER**
X	X	0.35
X	✓	0.40
✓	X	0.05
✓	✓	0.002

Table 3.2: Study: BER results versus time reversal and channel encoding

The system described in this thesis differ from previously attempted techniques due to increased self-imposed hardware limitations and by focusing on designing inherently robust signals. The specific hardware limitation restrict the system to approximately 320 Hz of bandwidth and a carrier frequency of 2048 Hz, drastically reduced bandwidth and center frequency relative to the previously referenced studies. The bandwidth limitation restricts the maximum achievable data throughput. A low carrier frequency enables longer distance communication. Additionally, the particular use of turbo coding for the channel encoder enables higher reliability in channels with severe interference.

3.2 Subcarrier Orthogonality

In this section, the orthogonality principle is described and its role in mitigating inter-symbol and inter-carrier interference is discussed.

Orthogonality is the principle that states the inner product of two signals is equal to zero. For multi-carrier communication systems, or specifically frequency shift keying, it describes the optimal frequency spacing and bandwidth allotted to each subcarrier tone to avoid interference, particularly inter-carrier interference (ICI), and maximize bandwidth allocation [18]. Maintaining orthogonality is important in environments with significant time variability and multipath arrivals. To remove the effects of ICI, the estimated Doppler spread, D_s, of the channel must be considered when determining the proper frequency positions of subcarriers, such that the frequency separation must be greater than the Doppler spread [19]. ICI occurs when the energy of a subcarrier leaks into adjacent subcarrier bands. Doppler shifts can change the subcarriers frequency enough to cause adjacent band energy leakage. The result is the system may lose its orthogonality due to ICI, thus deteriorating its performance. Referring back to equation (2.10) in Section 2.4, if all the path delays are less than the symbol period, and are each subject to a different Doppler shift, then each symbol path may experience different frequency shifts and interferers.

Figure 3.1 represents the phenomenon of inter-carrier interference due to severe time dilation or compression. As shown, a signal with a predefined frequency and

bandwidth undergoes the Doppler effect due to relative motion, represented by $f_{d,1}$ and $f_{d,2}$. The signal now shows frequency shifts and leaks into the subsequent band of its neighbouring subcarriers. Signals that were previously isolated with respect to frequency now overlap causing ICI.

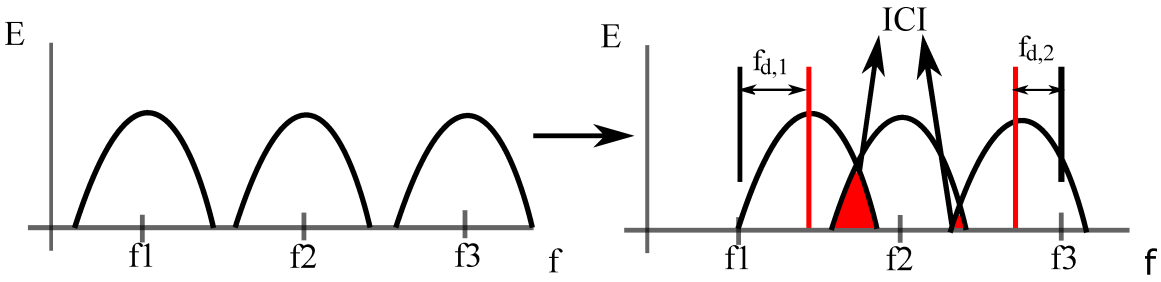

Figure 3.1: Inter-Carrier Interference Example

In a multicarrier modulation system, orthogonality between subcarriers allows the energy of each tone to be isolated within a specific sub-band. To achieve orthogonality between non-coherent subcarriers, their spacing must be integer multiples, n, of the inverse of the symbol period, T, as expressed by:

$$\Delta f = \frac{n}{T}. \tag{3.1}$$

Thus, the minimum frequency spacing is equal to $1/T$, (R_s), for $n = 1$. Figure 3.2 shows an example of the power spectral density of a BFSK modulation, where B_{n-n} is the null to null bandwidth of the symbol transmission. The left-hand side of the figure represents two signals that are separated by Δf that are inefficiently occupying the available band. The right-hand side shows the minimum frequency separation Δf_{min} the two signals can be separated by in order to maintain orthogonality.

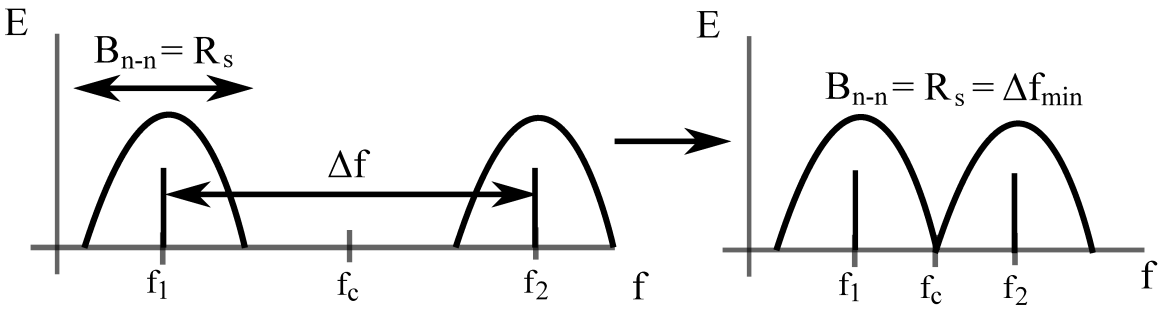

Figure 3.2: Frequency minimum for orthogonal BFSK

Having the frequency spacing between subcarriers greater than the Doppler spread of the channel ($\Delta f > D_s$) reduces the amount of energy that leaks into subsequent bands, ICI. Also, if the frequency spacing is greater than the coherence bandwidth ($\Delta f > B_{coh}$), simultaneous sub-band fading can be prevented. The coherence bandwidth, B_{coh}, is proportional to the inverse of the multipath delay spread, σ_t.

Inter-symbol interference (ISI) is the result of two or more symbols adding out of phase, the nature of this addition implies constructive or destructive fading. ISI can be caused by long propagation delay of multipath arrivals. Effectively, a previously transmitted symbol's echo may be received during the reception of the currently transmitted symbol. Referring back to equation (2.4) in Section 2.3, when a path's propagation delay, τ_p, is greater than the direct path delay, τ_0, ISI occurs. In underwater acoustic systems, τ_p may be much greater than τ_0. In this case, ISI may occur many symbols after the original symbols transmission.

Figure 3.3 represents the scenario of ISI in which the first symbol's reflection is received simultaneously with the second symbol. Two scenarios are shown, fully constructive and destructive interferences. This example is only shown for two consecutive symbols and represents an over-simplified single reflected path. If more than two symbols were transmitted, the effect of ISI would compound. It is apparent that the length of the latency in this scenario would have detrimental consequences for the third symbol as both the first and second symbols' reflections would distort its reception. The left hand side of the figure shows the transmission of two consecutive symbols with a period T given a propagation latency τ_0. In this particular example, a reflection of the first symbol is received with a path delay greater than the symbol period. The reception of this reflection occurs during the reception of the second symbol and causes ISI. Depending upon the phase of the interfering reflection signal, it can either cause constructive or destructive interference, as shown on the right hand side of the figure. When the addition of the multipath arrivals result in destructive interference, the signal amplitude may drop significantly. By ensuring the symbol period of the signal is greater than the delay spread of the channel then the effect of the transient amplitude fluctuations can be mitigated.

The effect of non-coherent ISI on a real signal is shown in Figure 3.4. The left

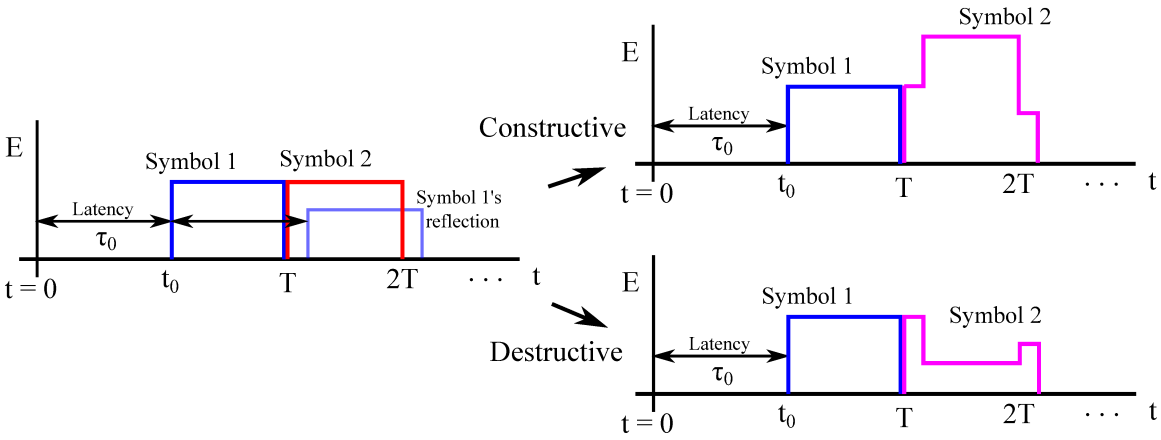

Figure 3.3: Inter-Symbol Interference Example

hand side represents a perfect multiple frequency shift keying (MFSK) signal, this is observed by the change in frequency of the signal every second. Notice on the right hand side, that although the amplitude of the signal is drastically reduced, after the first 0.2 seconds of the symbol, the signal amplitude becomes steady-state. The steady-state amplitude of the signal is important for removing noise and interference when performing energy detection through integration.

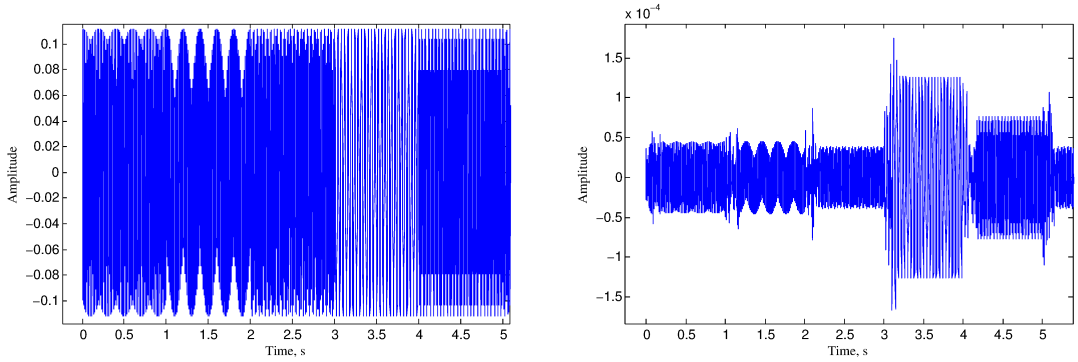

(a) Pure FSK signal

(b) ISI distorted FSK signal

Figure 3.4: Non-coherent addition of ISI on a real signal

3.3 Coherence

In this section, coherent and non-coherent systems are discussed. A brief description of their capabilities is described and their performance is compared.

Coherent communication systems exploit phase-tracking technology to improve the reliability of receivers. These receivers involve phase locked loops to measure and track the phase of the incoming signal and allow for improved data reception when compared to non-coherent systems. The improvement in reliability comes at a cost of increased receiver complexity and computation.

Alternatively, simple non-coherent receivers are easily implemented because the phase information is not required; but this sacrifices reliability. Non-coherent receivers typically employ energy detection for each subcarrier. A simple structure may be represented by downconverting, or bandshifting, using a common center frequency, low pass filtering, and parallel energy detection of subcarriers, shown in Figure 3.5. Energy detection is accomplished by further downconverting the received signal, R_x, by each subcarrier frequency, f_M, integration of the downconverted signal, and sampling before entering the decision device. This type of receiver is known as a correlation receiver [18].

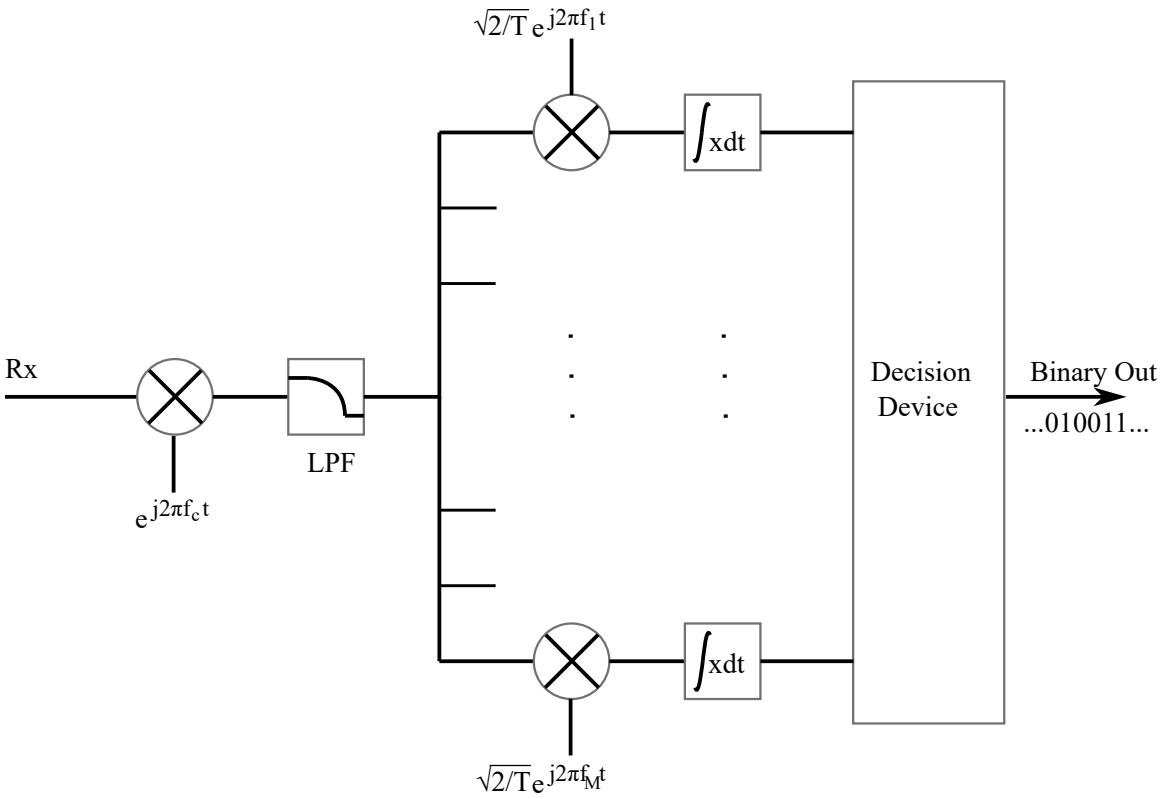

Figure 3.5: Non-coherent M-FSK receiver block diagram

Coherent receivers require additional circuitry to perform phase and carrier recovery. The increased complexity does offer a bit error rate (BER) improvement approximately equal to 3 dB when compared to non-coherent receivers, as shown in Figure 3.6. The non-coherent BER result was calculated using this theoretical equation:

$$P_{be-NonCoh} = \frac{M/2}{M-1} \sum_{n=1}^{M-1} \frac{(-1)^{n+1}}{n+1} \binom{M-1}{n} \exp\Big(- \frac{n(\log_2 M) E_b}{(n+1) N_0} \Big). \tag{3.2}$$

The probability of a bit error, P_{be}, is a function of the modulation order, M, the energy per bit, E_b, and the noise spectral density, N_0. Specifically, the energy per bit to noise spectral density ratio is equal to the bandwidth-normalized signal to noise ratio (SNR). The coherent BER result was generated using this following theoretical equation [18]:

$$P_{be-Coh} = \frac{2^{\log_2 M - 1}}{2^{\log_2 M} - 1} \Big(1 - \int_{-\infty}^{+\infty} \Big[Q\Big(-q - \sqrt{\frac{2 \log_2 (M) E_b}{N_0}} \Big) \Big]^{M-1} \frac{1}{\sqrt{2\pi}} \exp\Big(-\frac{q^2}{2} \Big) dq \Big). \tag{3.3}$$

The P_{be} results from these equations calculate the theoretical BER performance in an additive white Gaussian noise (AWGN) channel.

Additionally, coherent receivers allow for the use of phase-coded modulation schemes which offer higher bandwidth efficiencies, capable of achieving greater data rates with comparable bandwidths. In the presence of slow propagation delays, high channel variability, and significant multipath arrivals, phase correction signal processing techniques and implementations are considered complex. Although, systems incorporating coherent receivers and phase correction capabilities are being used today, specific underwater environments still pose signal processing challenges for these systems. With a focus on simplicity, overall robustness, and without the necessity for high speed communication, a non-coherent system satisfies the objectives.

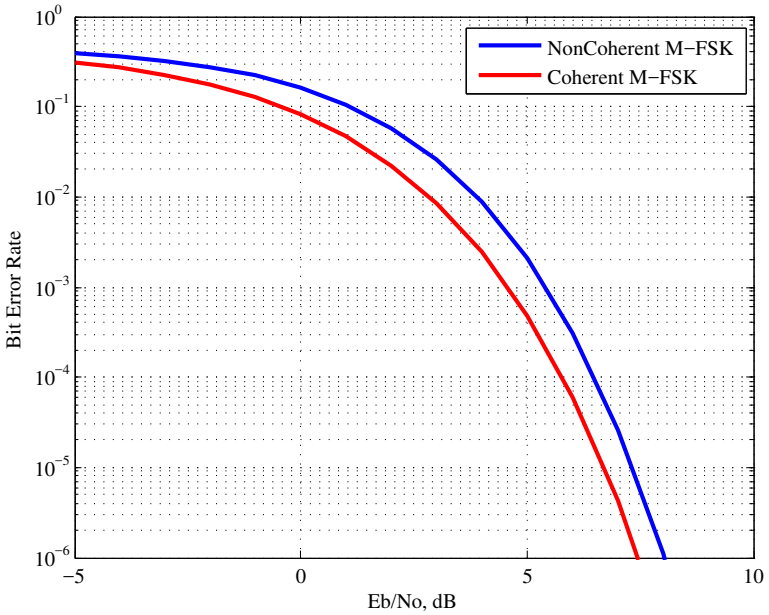

Figure 3.6: Coherent versus Non-coherent M-FSK BER

3.4 Long Range Non-Coherent Multicarrier Modulation Designs

In this Section, the design of two orthogonal, non-coherent, FSK modulations are described. The design of these modulation algorithms are constrained to hardware and propagation parameters.

An overview of the communication system is shown in Figure 3.7. The communication flow begins with binary information getting passed to the transmitter for modulation into a real signal. The real signal is transmitted through the wireless channel (distorted by multipath, Doppler, etc.) and is received at a remote receiver fixed in the middle of the water column. The receiver demodulates the signal, which is distorted by the acoustic environment, and produces an estimation of the transmitted binary information.

In Section 3.4.1, the standard tonal-based MFSK modulation scheme is described. Its simulation analysis is discussed in section 3.4.2. In Section 3.4.3, the proposed orthogonal, non-coherent, parallel BFSK modulation scheme is described, and its simulation analysis is discussed in Section 3.4.4.

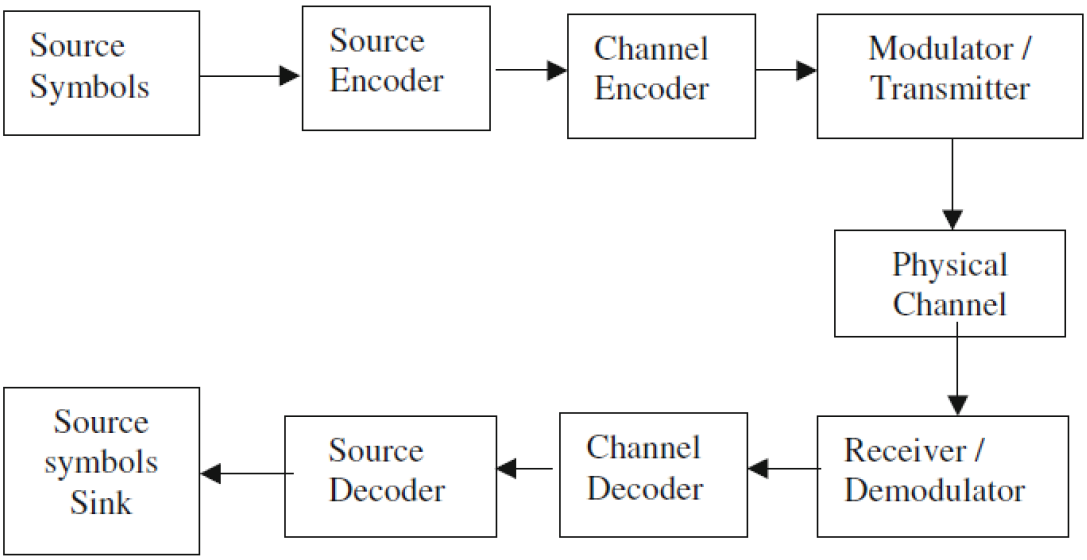

Figure 3.7: System Block Diagram

3.4.1 The Standard M-FSK

This section describes the methodology for designing, implementing, and simulating an M-FSK modulated signal.

Orthogonal MFSK modulation is a tonal based communication method that uses a fraction of the available bandwidth at any given time. Data is modulated at discrete subcarrier frequencies and one subcarrier f_i, where $i = [1 : M]$, is being transmitted at one moment in time for a specified duration, the symbol time, T_s. M is the number of subcarriers required and is known as the modulation order. M is determined by the number of bits transmitted per symbol, k, as defined by:

$$M = 2^k, \qquad R_b = \frac{k}{T_s}. \tag{3.4}$$

A real MFSK signal can be generated by a simple cosine:

$$s_i(t) = A\cos(2\pi f_i t + \theta), \qquad 0 < t \leq T_s, \tag{3.5}$$

where A is the signal amplitude, θ is the signals phase, and the frequency f_i switches

to a new subcarrier frequency after the symbol period, T_s, has elapsed. For non-coherent MFSK signals, the phase, θ, is disregarded during demodulation. The rate of transmission, R_b, is equal to the number of bits per symbol divided by the symbol period. As was discussed in Section 3.2, the maximum null to null bandwidth occupied by each subcarrier must be equal to or less than the frequency separation of subcarrier. Therefore, the total available bandwidth W must be divided into M equal segments, as defined by:

$$W = M \cdot \Delta f, \tag{3.6}$$

where Δf is the frequency separation between subcarriers. Provided a strict amount of bandwidth and adhering to the properties of orthogonality to reduce the ISI and ICI, a maximum number of subcarriers can be calculated.

The values for the total bandwidth and carrier frequency of the signal are chosen to represent the parameters for an underwater communication link and constrained on the hardware specifications. The total bandwidth, W, is equal to 320 Hz centered at a carrier frequency, f_c, of 2048 Hz. Next, one must choose the optimal frequency spacing to obtain the number of subcarriers that will be used. Recalling from Section 3.2, the frequency spacing must be greater than the Doppler spread to mitigate ICI. Additionally, the symbol time must be greater than the multipath delay spread to mitigate ISI. The multipath delay spread can be estimated from a Bellhop simulation as shown in Figure 2.6 and is equal to approximately 0.18 seconds.

The Doppler spread is typically extracted by evaluating the largest Doppler shifts that will be present within the system. High velocity vehicles need to account for large Doppler shifts. High velocities may cause excessive power leakage into adjacent bands due to these frequency shifts. If the platform's speed is constant, the resulting Doppler shift can be compensated by correcting the carrier. Assuming the system is static, relative motion between platforms may be minimal. In this scenario, Doppler spread is dominated by the variability of the ocean environment, particularly surface motion. For static platforms, an estimate for Doppler spread due to channel motion can be calculated by [20]:

$$D_s = 0.0175(f_c/c_w)w^{1.5}\cos\theta_p, \tag{3.7}$$

where, θ_p is the surface incident angle of the pth path arrival, w is the wind speed, f_c is the signals center frequency, and c_w is the sound speed. Assuming an incident angle of 45 deg, and a wind speed of 50 km/h, the estimated total Doppler spread is equal to 0.87 Hz, well within the tolerance of the 10 Hz frequency separation.

For a long-range design, to accommodate the multipath delay spread and the Doppler spread, a symbol time of 1 second is chosen, $T_s = 1$. A symbol time of 1 second is significantly larger than the delay spread, as simulated by the Bellhop model. The symbol rate, R_s, of the signal is the inverse of the symbol time and is equal to 1 symbol per second. A frequency separation of 10 Hz sufficiently satisfies the condition to mitigate ICI due to Doppler spread and provides limited protection against mobile Doppler shifts. A 10 Hz separation adheres to the orthogonality property ($\Delta f = nR_s$) by an integer multiple of $n = 10$. Therefore, for $W = 320\ Hz$ the total number of subcarriers that may be used in our predefined system is equal to 32. Also, having the number of subcarriers formed from base 2 simplifies modulation. The number of bits per symbol, k, in this system is calculated to be equal to 5 from Equation 3.4, for a bit rate, R_b, equal to 5 bps. A summary of the signal specifications is seen in Table 3.3. Figure 3.8 shows an example of the signal transmission of several symbols in the chosen spectrum.

Parameter	**Value**	**Constraint**
Carrier Frequency, f_c	2048 Hz	Hardware
Available Bandwidth, W	320 Hz	Hardware
Symbol Time, T_s	1 s	Channel
Frequency Division, Δf	10 Hz	Channel
Number of Subcarriers, M	32	Δf and W
Bits per Symbol, k	5 Bd	M
Bits per second, R_b	5 bps	T_s and k

Table 3.3: 32-FSK Signal Specifications

The M-FSK transmitter is shown in Figure 3.9. The incoming binary information gets separated into blocks equal to the number of bits to be transmitted per symbol. The value of each information block is mapped to a unique subcarrier frequency. Once

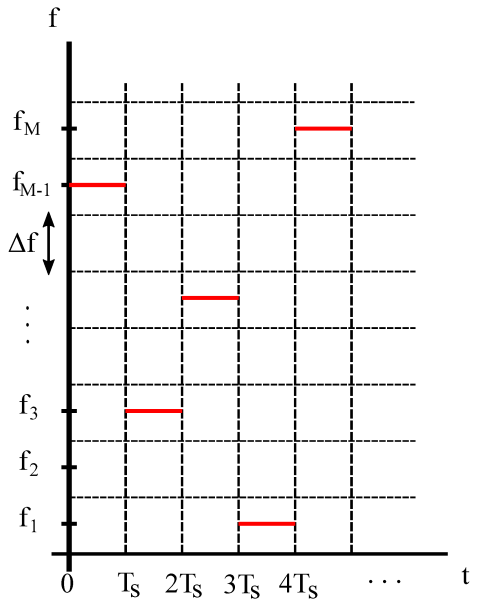

Figure 3.8: M-FSK symbol transmission

the subcarrier frequency is chosen, the baseband signal gets generated and passed through a pulseshaping filter to limit the switching bandwidth. The bandlimited signal is upconverted by the carrier frequency and converted into a real, passband, analog signal ready to be amplified and transmitted through the transducer.

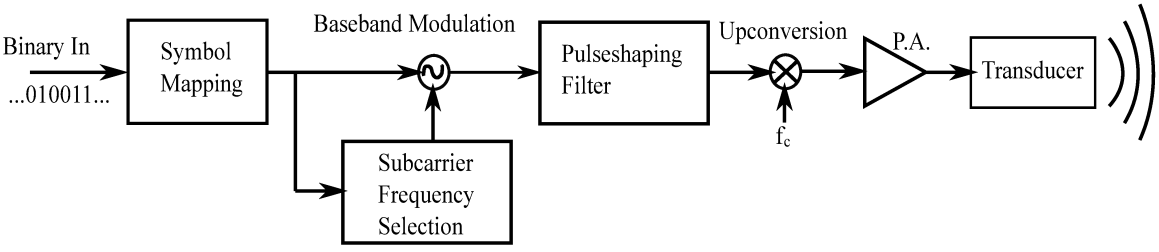

Figure 3.9: Modulator/Transmitter Block Diagram

In order to estimate the performance of the system in harsh underwater conditions, MATLAB simulations are used. The transmitter is simulated using a random number generator to represent data, which is then converted to a real signal to be applied to the front-end circuitry. The receiver algorithm is implemented to represent a non-coherent receiver depicted schematically in Figure 3.5. The simulation procedure, analysis, and results are discussed in Section 3.4.2.

3.4.2 32-FSK Simulation

Models of the transmitter, wireless channel, and receiver are implemented with MATLAB. The procedure consists in providing simple, yet realistic, subsea conditions through an iterative and incremental design procedure. First, to confirm the validity of the model, the BER is evaluated in controlled conditions and compared against a known theoretical performance in AWGN conditions. Secondly, the impact of multipath arrival is evaluated using channel impulse response shown in Figure 2.6. As such, the model now represents a static multipath ocean environment. To increase complexity further, time variation can be added to the channel, but since the Doppler spread is expected to be much smaller than the frequency separation equal to 10 Hz, it is expected that its impact is negligible.

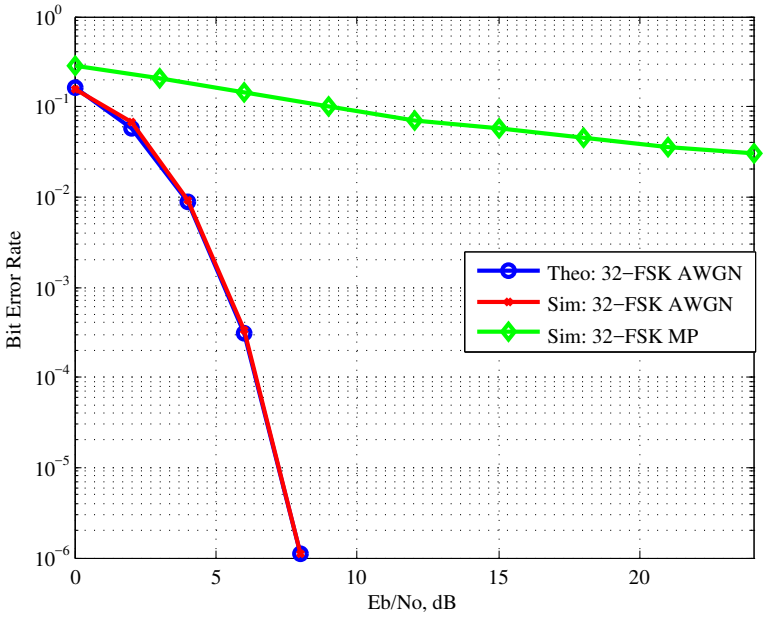

Figure 3.10: Simulation BER results for 32-FSK in AWGN and multipath

Figure 3.10 shows the BER of 32-FSK in an AWGN and multipath channel compared to the AWGN theoretical performance. Observe the reliability degradation due to the introduction to multipath. This deterioration is due to the non-coherent addition of multipath arrivals, which causes channel amplitude fading. During the simulation, 5000 1000-symbol frames are transmitted for a total bit count of 25,000,000 bits. The theoretical limit shown is calculated using Equation (3.2) for orthogonal

non-coherent M-FSK.

One can conclude from the initial simulation that the effect of steady-state flat fading deteriorates the system significantly. Further work needs to be done to improve the performance in a harsh multipath environment.

3.4.3 Parallel BFSK

This section describes the methodology for designing, implementing, and simulating a multi-parallel tone BFSK modulated signal.

As an alternative to the standard M-FSK proposed in Section 3.4.1, tones transmitted in parallel may offer improved data rates without major degradation in robustness. Similar to orthogonal frequency division multiplexing (OFDM), parallel FSK tones can more efficiently occupy the alloted bandwidth than a single FSK tone. Limited by the same specifications for the 32-FSK system including orthogonality and non-coherent signaling, a 16-parallel BFSK system is proposed. Specifically, here sixteen binary-FSK tones are sent simultaneously to achieve a higher bit rate without adding complexity and with minimal sacrifice to reliability. This modulation scheme improves the bandwidth efficiency by occupying half of the available 32 subcarriers at any given time, as opposed to one tone per symbol period in MFSK. The bit rate of the parallel system is equal to the number of parallel tones being transmitted P multiplied by the number of bits modulated per tone, k. Modifying Equation (3.4), k is equal to the log base 2 of M and P is equivalent to the number of available subcarriers divided by the chosen modulation order:

$$k = log_2(M), \qquad P = \frac{M_{sub}}{M} \tag{3.8}$$

where,

$$R_b = \frac{kP}{T_s}. \tag{3.9}$$

Consequently, the modulation order of the system must decrease to support the transmission of parallel tones. In an AWGN channel, the performance of an FSK system is dependent on its modulation order. Thus, determining an appropriate value for the number of parallel transmissions is a choice between improved bit rate versus reliability, as shown in Table 3.4.

# of Parallel Tones	**Modulation Order**	**Bit Rate**	**Robustness**
1	32	5	High
2	16	8	Medium-High
4	8	12	Medium
8	4	16	Medium-Low
16	2	16	Low

Table 3.4: Parallel Tone, Modulation Order Comparison

A lower reliability, higher throughput modulation type is chosen to analyze the performance of the parallel tone modulation algorithm. This serves to measure the performance degradation with respect to bit rate increase. Table 3.5 provides the signal specifications for the new 16-parallel BFSK scheme. An example of several consecutive symbol transmissions is shown in Figure 3.11. Note that using parallel BFSK, half the subcarriers are being occupied at any given time.

Parameter	**Value**	**Constraint**
Carrier Frequency, f_c	2048 Hz	Hardware
Available Bandwidth, W	320 Hz	Hardware
Symbol Time, T_s	1 s	Channel
Frequency Division, Δf	10 Hz	Channel
Number of Subcarriers, M_{sub}	32	Δf and W
Modulation order, M	2	M_{sub} and P
Number of Parallel Tones, P	16	M_{sub} and M
Bits per Symbol, k	16 Bd	M and P
Bits per second, R_b	16 bps	T_s and k

Table 3.5: 16-Parallel BFSK Signal Specifications

An advantage of the parallel tone modulation is that it utilizes similar transmitter and receiver structures as for single tone modulation techniques. The transmitter, shown in Figure 3.12, generates and adds P baseband signals in a loop. Pulseshaping may be accomplished on each individual baseband signal and is then used as a feedback. When all parallel tones are generated, the signal is then upconverted and

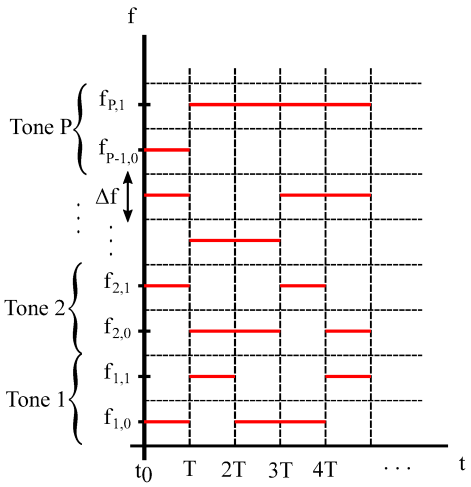

Figure 3.11: Parallel BFSK symbol transmissions

amplified through a single transducer. The receiver structure for parallel transmissions is similar to that of the single tone and also utilizes a similar decision device since energy is being detected on every subcarrier. Specifically, for the single tone decision, the subcarrier that accumulates the most energy is decoded as the most likely transmitted symbol. For parallel BFSK transmissions, the decision is made for each parallel subcarrier pair (i.e. for 16-parallel tones, 16 decisions are made by choosing the higher energy subcarrier for each parallel subcarrier pair).

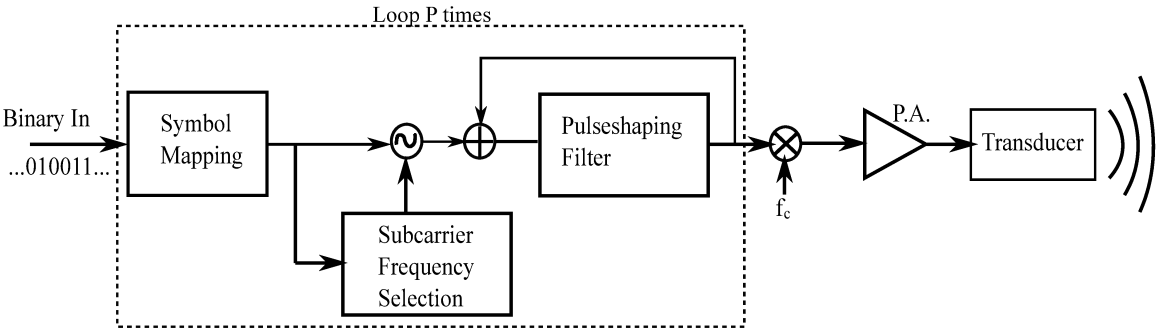

Figure 3.12: Modulator/Parallel-tone Transmitter Block Diagram

3.4.4 16-Parallel BFSK Simulation

To assess the performance of 16-parallel BFSK, similar to Section 3.4.2, a 16-parallel BFSK waveform is generated and passed through an AWGN and a multipath channel while being compared to the theoretical limit for a BFSK signal in an AWGN channel.

The theoretical BER result is calculated using the non-coherent probability of a bit error as defined by Equation (3.2) where M is set to be equal to 2. The probability of bit error equation simplifies significantly and is expressed as:

$$P_{be-BFSK} = \frac{1}{2}\exp\Big(-\frac{E_b}{2N_0}\Big). \tag{3.10}$$

These simulation results are produced by transmitting 500 1000-symbol frames where each symbol contains 16 bits, a total of 8,000,000 bits. The results of the simulation showing the theoretical BFSK BER in AWGN, 16-parallel BFSK in AWGN, and 16-parallel BFSK in AWGN and multipath is shown in Figure 3.13. Similarly to the 32-FSK results, the 16-BFSK BER performance in a multipath channel deteriorates significantly. Although, it can be seen from the simulation that adding parallel tones to the waveform do not negatively impact the AWGN performance.

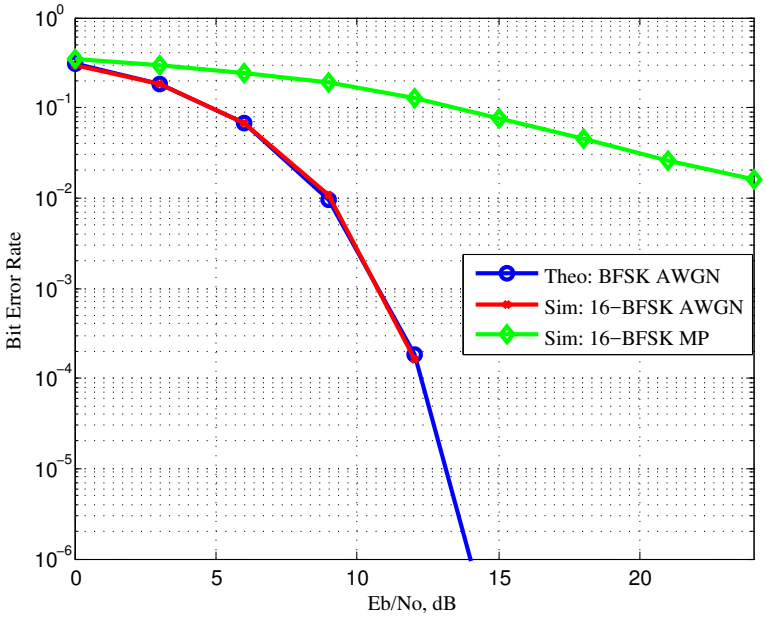

Figure 3.13: Simulation BER results for 16parallel-BFSK in AWGN and multipath

However, when comparing the 16-BFSK BER results with the 32-FSK BER results in an AWGN channel, a degradation in performance is seen, as shown in Figure 3.14. This performance degradation is due to a difference in modulation order. To achieve a comparable AWGN BER performance of 10^{-5} with 16-parallel BFSK, 5 dB more

signal power is required. Although more energy is required to achieve similar levels of robustness in AWGN, the 16-BFSK modulation provides $3\times$ the data throughput.

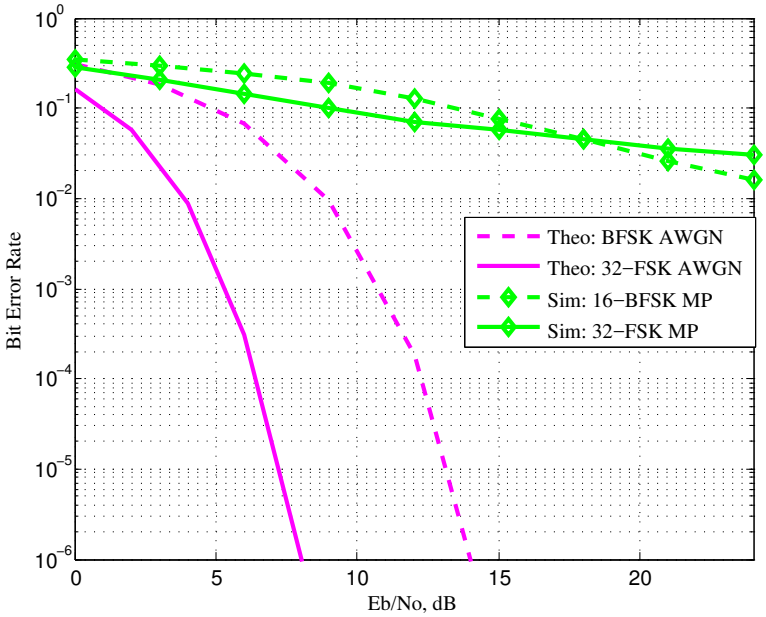

Figure 3.14: Simulation BER comparison for 16-BFSK and 32-FSK in multipath

Observing the multipath performances, both modulation schemes offer similarly high BERs and are currently unsuitable for reliable communication.

3.5 Spreading Techniques

In this section, spreading techniques are described to increase robustness for communication links in harsh environments. This section describes frequency hopping spread spectrum and the forward error correction technique known as turbo code.

Spreading techniques may slow the data rate or utilize extra bandwidth of the communication link in exchange for robustness gain in channels with extreme ISI. They may be used in situations that require low SNR by spreading signal power over frequency or time and can also be used to employ multi-user networks [19]. Systems that employ coherent modulation schemes such as phase-shift keying, PSK, may use a spread spectrum technique called direct-sequence spread spectrum, DSSS [15]. DSSS involves increasing the systems symbol rate by a factor of N. The increase in symbol

rate spreads the energy of the single carrier signal over a bandwidth N times larger. In these systems, N is referred to as the processing gain or spreading factor. The larger bandwidth helps mitigate performance degradation due to narrowband interference. For FSK systems, frequency hopping spread spectrum, FHSS or FH, is the most commonly used spread spectrum technique and will be discussed in section 3.5.1. For the current application, the use of spread spectrum techniques was investigated to assist in ISI mitigation.

3.5.1 Frequency Hopping Spread Spectrum

This section presents the frequency hopping spread spectrum (FHSS) methodology, signal design, and simulation results.

Frequency hopping may spread the signal in frequency and time to mitigate the effects of variable multipath and impulsive noises. There are two types of FHSS techniques, fast FHSS and slow FHSS. In fast FHSS, symbols are divided into N chips with duration T_c (3.11). For slow FHSS, chips consist of multiple symbols. Fast FHSS is most commonly used as it has better impulsive noise mitigation characteristics.

$$T_c = \frac{T_s}{N} \tag{3.11}$$

To employ frequency hopping, the available bandwidth needs to be divided into specific hopping bands. The number of available hopping bands, L, is independent of the spreading factor, N. To achieve high reliability with FH schemes, the optimal value for both, L and N would be as high as possible. However, there are limitations to these values. The chip period, T_c is constrained to be greater than the multipath delay spread. Therefore, large spreading factors which equates to many chips per symbol can drastically increase the symbol period and significantly reduce the bit rate of the system. The number of available hopping bands is derived based on the amount of available bandwidth, W, as mentioned in equation (3.12). The largest value L can achieve in the described system is 16 while transmitting a BFSK signal. In FHSS systems with more available bandwidth, there are a higher number of hopping

bands to increase robustness.

$$W = L \cdot M \tag{3.12}$$

Figure 3.15 shows a transmission diagram of a FH BFSK signal. The signal can hop to L bands with a hop spacing of W_L and hops twice per symbol, $N = 2$. After the signal undergoes despreading, it resembles a typical BFSK signal. The hopping pattern must be known at the transmitter and receiver to spread and despread the signal, respectively. For multi-user applications, each user employs a polynomial seed to generate a sequence that appears pseudo-random but maintains good cross-correlation properties.

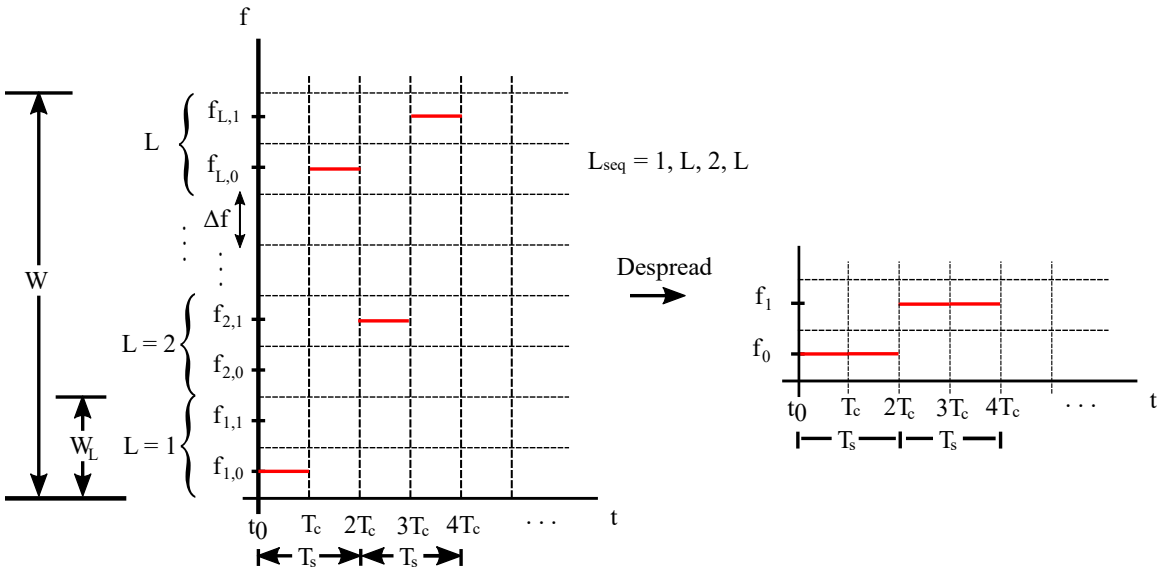

Figure 3.15: Frequency hopping BFSK transmission diagram

As a consequence of requiring the most available bandwidth to support the FH technique, the previously discussed modulation algorithm of parallel BFSK is not supported.

3.5.1.1 FHSS Simulation

Two simulations were generated to test the reliability improvement by using FHSS. Since the use of FHSS in this application will not be tested in a multi-user system

but will be tested in its ability to mitigate ISI, a random generator was used to generate the hopping sequence. Table 3.6 lists the specifications of the simulated FH signals. The number of available hopping bands was set equal to 16 to achieve the highest reliability measure possible for this system while maintaining the minimum frequency spacing. A value of 10 and then 100 was set for the number of chips per symbol resulting in extremely low data rates.

Parameter	**Value**	**Constraint**
Number of Subcarriers, M_{sub}	32	Δf and W
Modulation order, M	2	M_{sub} and P
Number of hopping bands, L	16	M_{sub} and M
Chip Time, T_c	1 s	Channel
Chips per symbol, N	10, 100	—
Symbol Time, T_s	10 s	T_c and N
Bits per Symbol, k	1 Bd	M and P
Bits per second, R_b	0.1, 0.01 bps	T_s and k

Table 3.6: FHSS BFSK Signal Specifications

Figure 3.16 represents the simulation BER results comparison between 16-BFSK, 32-FSK, and both FH BFSK algorithms in a multipath channel. It is observed that applying the FHSS technique does mitigate the channel effects of ISI to provide reliable communication at high SNR. However, the data rates of these FH systems are currently too slow for practical use.

3.5.2 Forward Error Correction: Turbo Coding

This section discusses the implementation of turbo code; its encoder, its decoder, and its simulation results.

Forward error correction (FEC) techniques are used by employing redundant information to an information signal to improve reception performance of a communication system in noisy environments. The addition of redundant bits to a signal allows the signal to be decoded into the most likely transmitted codeword and improving the overall bit error rate of the system. The improvement of BER is at the cost of reducing the overall throughput of the system. FEC techniques are ideal wherever a robust reception is priority. There are several techniques to encode a signal. For the

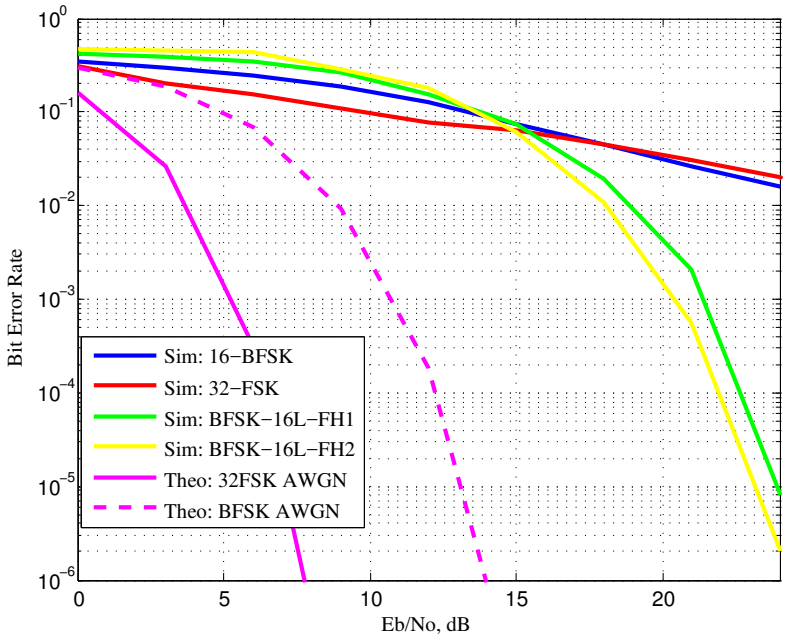

Figure 3.16: Simulation BER comparison for 16-BFSK, 32-FSK, FH-1 BFSK, and FH-2 BFSK in multipath

purposes of achieving high reliability, a turbo coded system was reviewed. Turbo code is a high performance FEC technique and is currently being used in 3G/4G mobile communication systems.

The turbo encoder uses two recursive systematic convolutional (RSC) encoders combined with an interleaver. The complexity of the encoders depend on the designed constraint length. The larger the constraint length the more computationally expensive but reliable decoding process. The constraint length is dependent on the number of memory elements of the particular encoder. The encoders employ a specific generator matrix to determine structure and complexity of the encoder, this matrix is known at the transmitter and receiver. The use of RSC encoders in turbo code improve the rate of the encoder when compared to non-recursive, non-systematic encoders. This particular turbo encoder, shown in Figure 3.17 has a rate of 1/3 (input bits/output bits). The interleaver shuffles the input sequence to improve the performance of the encoder against noisy burst errors. The interleaver output then gets encoded with the second RSC encoder. The output of the turbo encoder gets modulated and transmitted through the channel.

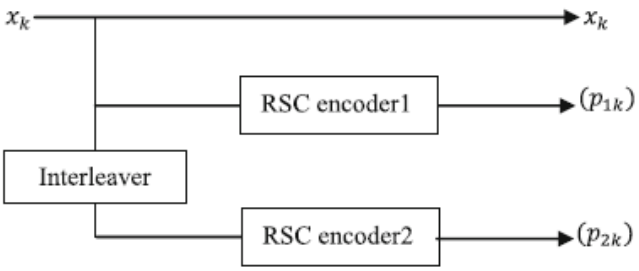

Figure 3.17: Turbo encoder block diagram

As information gets passed though the encoder, the memory elements update and change state. An initial condition for the encoder requires that the memory elements prior to encoding information must be in state 0. State 0 implies that every memory element is not biased and remains in the starting state. To ensure the encoder starts in state 0, termination bits must be transmitted at the end of the previous transmission to flush out any remaining memory. When the encoder is encoding information bits, the state of the encoder changes. The number of states in a convolutional encoder is equal to the number of memory elements to the power of possible values, since are information signal is binary it is to the power of 2. A diagram of state to state transitions is known as a trellis. The trellis is formed when the information is encoded and has two initial conditions that are known to improve the decoding process. The initial conditions ensure that the initial state of the encoder must be in state 0 and that the terminating state must also be in state 0. Additionally, in order for the decoder to function, the structure of the encoder must be known at the decoder. This is necessary to calculate state to state transition properties during decoding.

The turbo decoder uses two decoding blocks that feed extrinsic information between each other. The feedback and feedforward implementation of the turbo decoder allows an iterative improvement in performance at the expense of computational processing. The block diagram of the turbo decoder is shown in Figure 3.18. Each decoder runs a BCJR algorithm, which is named after its inventors Bahl, Cocke, Jelinek, and Raviv [21]. It is a forward/backward recursive MAP, Maximum A Posteriori, algorithm that produces an estimated log-likelihood ratio, LLR, probability of the received sequence. The algorithm uses information based upon the signal to

noise ratio from the channel and extrinsic information passed from the corresponding decoder. This extrinsic information is an error estimation which improves after each iteration through the decoder. The output of each decoder block and turbo decoder itself is a log-likelihood ratio vector, the sign (+/-) of the LLR determines the predicted input (1/0) with its magnitude representing a confidence level.

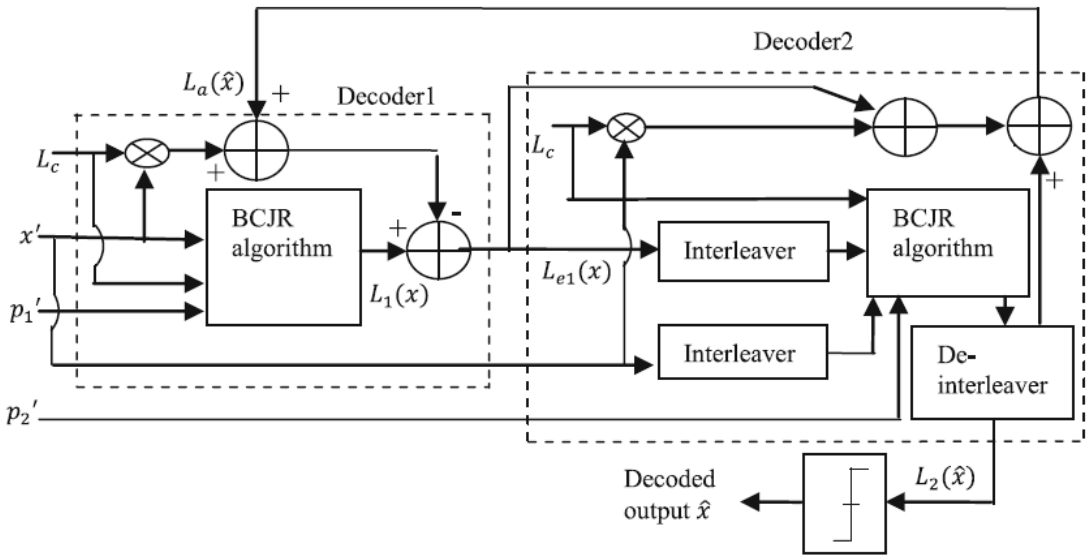

Figure 3.18: Turbo decoder

Introducing the BCJR algorithm, the LLR values are computed using three different variables. Each of the variables, alpha α, beta β, and gamma γ, correspond to predictable processes at varying times (i.e. past, future, and present, respectively). Since the gamma variable depends upon current conditions (such as SNR value, state to next state transitions, and input signal) it is the first variable to be calculated. Both of the other variables, alpha and beta, depend upon gamma in their calculations. The equation used to calculate the value of gamma:

$$\gamma = P_{AP}\Big(\frac{1}{\sqrt{2\pi\sigma^2}}\Big)^n \exp\Big(-\frac{1}{2}\frac{\sum(x-\mu)^2}{\sigma^2}\Big). \tag{3.13}$$

Where P_{AP} is the A Priori Probability, σ^2 is the signal variance, μ is the expected symbol outcome or mean, and x is the input symbol. Note that the input symbol, x, to this equation is the received symbol corrupted by the AWGN and ISI channel.

Therefore, the value of the SNR affects the input symbol and the value of the variance. The mean, μ, is determined by the expected output of the current state. The value of P_{AP} is equal to 0.50 for binary information.

Following the calculation of the gamma variable, either alpha or beta can be computed next since they do not depend on one another. The alpha variable depends on the past, or previous state transitions. By knowing our initial state, state 0, this information is used to setup an initial condition. Using this initial condition and the previously calculated gamma values, iterative calculations find all the alpha values. Subsequent alpha values depend on its previous value. The equation for calculating the alpha values can be seen using the initial condition $\alpha_0(0) = 1$, and 0 otherwise:

$$\alpha_t(s_t) = \sum_{s_{t-1}} \sum_{a} \alpha_{t-1}(s_t - 1)\gamma_{t-1,t}(s_{t-1}, a, s_t). \tag{3.14}$$

The beta calculation is similar to the alpha calculation, but in reverse. Beta is a variable that depends on future states, therefore the initial condition depends on the state the system finishes in. By adding a stop sequence on the input signal, this ensures that the system always ends in a known state, such as state 0. Using this information, a secondary initial condition can be defined. Similarly to the alpha calculation, beta depends on its future value and the previously calculated gamma. However, since beta depends on future values, its calculation is done in reverse, this can be seen in equation (3.15). Initial condition $\beta_N(0) = 1$, and 0 otherwise:

$$\beta_{t-1}(s_{t-1}) = \sum_{s_t} \sum_{a} \beta_t(s_t)\gamma_{t-1,t}(s_{t-1}, x, s_t). \tag{3.15}$$

For both of the equations, the inside summation is for the possible input values, a, which represents a binary input. The second, outside, summation is for all possible states, s. For alpha, only previous states are possible, and for beta, only future states are possible. The output of the BCJR decoder, and ultimately the turbo decoder, is the LLRs, log-likelihood ratios. LLRs are statistical values to evaluate the probability of the the most likely sent signal. They are calculated after all previous variables have been found. The equation for determining the LLRs is shown below:

$$LLR(s_{t-1}, s_t, a) = \alpha_{t-1}(s_t - 1) \times \gamma_t(s_{t-1}, s_t) \times \beta_t(s_t). \tag{3.16}$$

The turbo decoder goes an extra step by feeding the resultant LLR values as initial conditions between both BCJR algorithms and producing an error estimate. The error estimate is fed into the second BCJR algorithm to improve the result of the estimate information sequence. A turbo decoder can iterate through this error estimation process until performance gain is considered negligible.

3.5.2.1 Turbo-Coded Simulation

The turbo code was implemented in MATLAB and combined with 32-FSK, 16-BFSK, BFSK-FH1, and BFSK-FH2. The turbo encoder used is simple in nature, involving only 2 memory elements, thus producing 4 states. The frame length used to generate the trellis path was equal to the frame length for each previous simulation, 1000 symbols. The performance of the turbo code is greatly influenced by the complexity of the encoder (number of states), the length of the frame, and the number of decoding iterations. The more complex, the longer the frame, and more iterations all improve the estimation capabilities of the decoder until the decoder can no longer improve its estimation. For the purposes of the simulation, 5 decoder iterations were used. The simulation results are shown in Figure 3.19. Note, that since the turbo encoder uses a rate of 1/3, the data rates of the encoded algorithms are reduced by a factor of 3. Previously, the 16-tone parallel BFSK modulation provided 16 bps, after encoding, will only provide 5.33 bps.

The improvements in BER due to the implementation of turbo code provides a usable and reliable communication algorithm for each of the previously mentioned modulation schemes. From the results of this simulation, the performance of 32-FSK and 16-BFSK improve the most and greatly approach their AWGN performance while in a multipath channel. The two frequency hopping algorithms increased their performance by the least while providing the slowest data rate. The best performing algorithms in simulations thus far are the standard 32-FSK and the 16-tone parallel BFSK, providing good reliability and usable data rates.

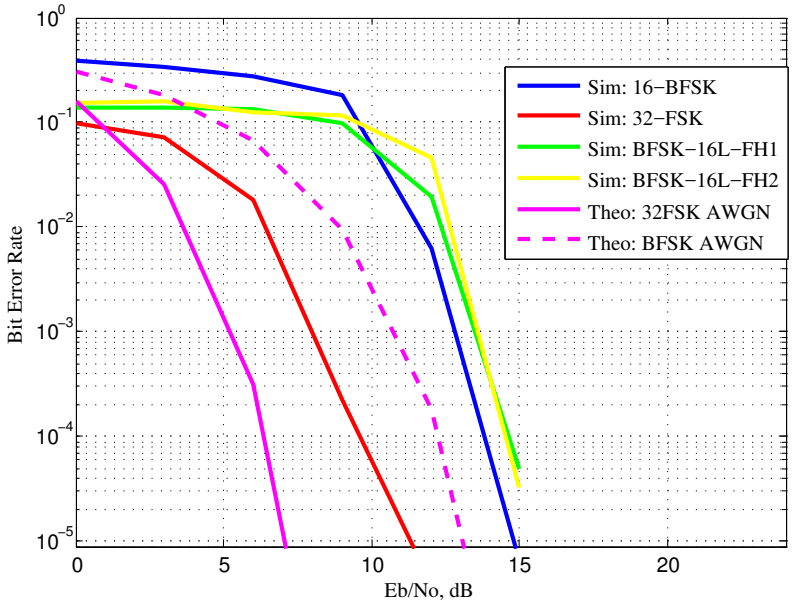

Figure 3.19: Turbo code BER results in multipath

3.6 Application: JANUS

In this Section, JANUS is reviewed and its specifications are described. Its modulation techniques are comparable to the techniques designed later in this thesis.

The JANUS protocol is the first global standard for digital underwater communications and is recognized by NATO to break the interoperability barrier and for collaborative underwater communications [23]. Dissecting this protocol makes a wide range of applications feasible [24], such as sending and receiving AIS and distress signals among tactical surveillance submarines, autonomous underwater vehicles (AUVs) and surface vessels that operate acoustic modems running the JANUS protocol.

In the JANUS standard specifications, binary data is converted to a continuous waveform with center frequency of f_c= 11520 Hz, B_W = 4160 Hz for typical communication operational scenarios [25]. In the JANUS standard, 13 pairs of orthogonal tones are mapped in evenly-spaced tone pairs that span the acoustic frequency band bandwidth, and is nominally 1/3 of the center frequency. A fixed preamble sequence of 32 chips is also defined for detection and synchronization with no space between

the preamble and the main JANUS packet [26].

The JANUS base packet is 64 bits, consisting of a 34-bit application data block (ADB) determined by the acoustic node. The ADB first 8 bits are for channel reservation and beacon and the remaining 26 ADB bits are node information. Each node can specify what information is encoded and how it is encoded into the 34 node-available ADB bit. The JANUS bit stream will be assembled according to bit allocations in Figure 3.20.

Protocol Version	Mobility Flag	Scheduling Bit	Tx/Rx	Forward Capability	User Class	Application Type	Repetition	ADB		CRC
								Reserved or Repeat interval	Node Information	
4	1	1	1	1	8	6	1	7	26	8

Figure 3.20: JANUS Packet bits 1 to 64

After assembling the JANUS payload, an 8-bit cyclical redundancy check (CRC) is added to the stream to detect the data corruption. The system also employs a 1/2 rate convolutional encoder [27] that is applied to the 64 bits of JANUS packet and is intended to combat the channel multipath interference as well as fading. Prior to encoding, 8 zero bits are appended to the 64 bits data so that the encoder can encode the next block correctly, these are the encoder termination bits. The total number of symbols output by the encoder then becomes $2 \times (64 + 8) = 144$ symbols applied to the modulator. Frequency-Hopped Binary Frequency Shift Keying (FH/BFSK) is the chosen modulation scheme.

Chapter 4

Ocean Experiments

A sea trial was run in St-Margaret's Bay, Nova Scotia on July 26-28 2017 to test underwater communication algorithms. The overarching goal was to demonstrate the communication performance of new algorithms in controlled underwater acoustic environmental conditions. Prior to the trial, several tests were run on land and at sea to calibrate the hardware. The objective of these calibration tests is to demonstrate the performance of key physical-layer sub-systems in realistic underwater deployments before the sea trial.

In Section 4.1, the hardware of the system is described for the transmitter and receiver. Section 4.2 discusses the system calibration procedure. Section 4.3 describes the procedure, deployment, and experimental results of the sea trial.

4.1 Front-End Hardware Design

In this section, the transmitter architecture and specifications are described. The power amplifier and transformer are characterized and evaluated. The receiver, a 5 element vertical line array that was obtained from Turbulent Research, is discussed.

The transmitter architecture is shown in Figure 4.1. The transmit signal from the sound card is provided over a mono single-ended interface. A class D-power amplifier is used and includes a pulse width modulator to convert the analog output from the jack to digital pulses, a power amplification stage driven differentially, and a filter to recover the signal envelope. The output of the power amplifier is further applied to a step up transformer to multiply the voltage by a factor of n. The output of the transformer is applied to the projector. To maximize the power transfer at the output the power amplifier, a matching network may also be implemented to present

an equivalent impedance of 4 Ω at the output of the PA, however, this matching network was not implemented. The transmitted audio signal was converted into sound files, and played using a laptop. The quality of the sound depends on the audio card specifications. Typically, the sound card provides 44.1 kHz sampling rate with a 16-bit quantization DAC.

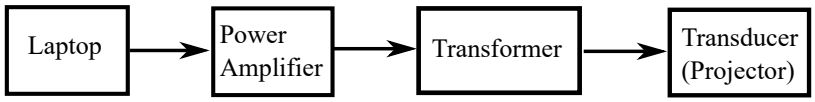

Figure 4.1: Transmitter Architecture

To vary the output power for different test ranges, the volume produced by the sound card is adjusted. The projector is a flexural disk projector (bender) approximately 5-inches in diameter and about 1-inch thick (potted size). The projector operates in the 1.5 kHz to 2.5 kHz range and can be driven with a maximum voltage of 1000 VRMS. To ensure sufficient SNR is obtained at the desired transmission ranges, a simple propagation calculation was performed. The sensitivity of the receiver is -165 dBm re 1 $\mu Pa/V$. To define the underwater ambient noise power spectral density (PSD) a model described by Urick can be used [3]. For low shipping activity, and wind speed on the order of 10 m/s, the total PSD due to flow noise, shipping activity, surface noise, and thermal noise is estimated to be 67 dBm/Hz. Assuming a simple cylindrical spreading model, one obtains a one-way transmission loss (TL) of 80 dB for a 10 km range with a frequency of 2 kHz. Then, for a signal bandwidth of 320 Hz and imposing an SNR requirement of 20 dB to ensure sufficient signal quality, the required audio transmit source level in dBm re 1 μPa @ 1 meter is:

$$SL = (67 + 10\log(320) + 80 + 20) = 192 \text{ dBm re } 1\mu\text{Pa} \tag{4.1}$$

The transmit voltage response (TVR) for the projector is 137 dB re 1 $\mu Pa/V$@1 meter at the resonant frequency. Also, the projector admittance at the resonant frequency is $Y = 0.4 + j0.8mS$. Using the TVR of the projector, the voltage required at the input of the projector is on the order of $10^{(192-137)/20} = 565VRMS$. To drive the conductance $G = 0.4mS$, the power required is equal to $P = V^2 \times G =$

$565^2 \times 0.4 \times 10^{-3} = 128W$. Similarly, to propagate 1 km a 57 VRMS, 1.28 W voltage supply is required to achieve an SNR of 20 dB.

4.1.1 Power Amplifier

In this Section, four off-the-shelf power amplifier specifications are compared to meet the transmitter power requirements. The power amplifier (PA) specifications are listed in Table 4.1.

Specifically, EPC's 9016 power amp is compared to a class D full bridge manufactured by International Receiver, Peavey's Crest 9200, and QSC's PL380. The EPC9106 evaluation board sold by Efficient Power Conversion Corporation (EPC) was originally considered because it was powered using power supplies available to the research team. However, it was soon realized that the number of turns is excessive for the low-voltage produced at the output of the EPC 9106. This also true for International Receiver's IRAUDAMP70. In comparison, both the Crest 9200, and the PL380 operate on a 120 VAC input, and as such can provide much more power in a standard load. The PL380 is the most efficient and delivers 5000 W in an 8 ohm load. Another advantage of the Crest 9200 and PL380 is that the two stereo channels can be bridged to provide a single output. This doubles the output voltage. For example, when the two channels are bridged, the Crest 9200 produces 188 VRMS while the PL380 produces 200 VRMS. Then, to produce the required transmit voltage, a turns ratio of 4:1 would be more than sufficient. Quotes were requested for the both the Crest 9200 and PL380 from RaveAudio. Not only is the Crest 9200 much more expensive, it has a lead time of 8 weeks. The power amplifier of choice is QSC's PL380.

4.1.2 Transformer

In this Section, the transformer required to step up the voltage to achieve a transmission range of at least 10 kilometers is described.

The PL380 power amplifier provides a voltage on the order of 200 VRMS. The

Manufacturer	EPC	International Rectifier	Peavey	QSC
Part Number	9106	IRAUDAMP7D	Crest 9200	PL380
Configuration	Class-D Full Bridge	Class-D Full Bridge	Mono-bridge/Class H	Mono-bridge/Class D
Power Supply	p/m 30V	p/m 30V	120 VAC	120 VAC
Output Power	240 W @ 4 Ohms	500 W @ 8 Ohms	6500 W @ 4 Ohms	8000 W @ 4 Ohms
Voltage RMS: 4 Ω/Stereo	-	-	93.8	100
8 Ω/Stereo	-	-	101.98	109.54
4 Ω/Bridge	30.9	-	161.2	178.8
8 Ω/Bridge	34.6	63.2	187.6	200
Required Turns Ratio	18.2	9.96	3.35	3.15

Table 4.1: Power Amplifier Specification Comparison

voltage required to achieve a distance of 10 km, is equal to 565 VRMS. To step up the voltage to the required level, an integer turns ratio of $n = 3$ is required. Note that an ideal transformer will maintain the power consumption at the primary and secondary. Consequently, the current will be stepped down by a factor of $n = 3$, and the impedance will be stepped up by a factor of 9. Assuming a projector with an equivalent parallel resistance equal to 2500 Ω, the resistance seen by the power amplifier at the primary is equal to 278 Ω. As such the power delivered to the load will be 144 W and can be used to define the power supply specifications. Since the transformer specifications are not standard, a transformer with a turns ratio of 3 was created by Dalhousie's Electrical Technicians. To design an ideal transformer at the $f_c = 2.048$ kHz operating frequency, the primary inductor impedance $j\omega L$ must be much greater than the load impedance reflected at the primary, i.e. $j2\pi f_c L >> 278$.

4.1.3 Receiver

In this Section, the vertical line array (VLA) that was used as the receiver is described.

The receiver consists of 5 hydrophone elements specifically arranged to create a vertical array, shown in Figure 4.2. The spacing depends on the wavelength of the

signal of interest and is calculated as $\lambda = c_w/f_c$. Calculating an estimated wavelength for the system is equal to 73 cm. By spacing the hydrophone elements by $\lambda/2 = 36cm$, the signal correlation goes through a null. This supports the concept and application of diversity reception in multiple-input multiple-output (MIMO) systems.

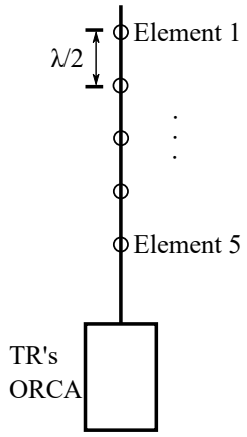

Figure 4.2: Vertical Line Array Diagram

The array of hydrophones connects to the Turbulent Research ORCA pressure case, which is designed to withstand the pressure at a depth of 100m underwater. The raw data measured from the hydrophones get sampled at a rate of $f_s = 24000$ Hz in 16 bit vectors (2 byte vectors). Knowing the sample rate and bit allocation per sample, the amount of memory required for a 3-day sea trial can be calculated, $Memory = 5 \times 24000 \times 2 \times 72 \times 3600 = 63$ GB. The internal memory on the OCRA is over 1 TB, therefore our memory requirement is satisfied.

4.2 System Calibration

The calibration was run in Bedford Basin near the DRDC Acoustic Calibration Barge, from a pontoon boat, rented through East Coast Watercraft Rentals. A Figure of the experimental setup is shown in Figure 4.3.

The calibration was run by sending short continuous wave pulses with a period of $T = 0.01s$ sweeping through the frequency band from 1800 Hz to 2300 Hz in 50 Hz steps. The length of the pulse was constrained to avoid multipath interference from the surface reflected path. The TVR is evaluated using post-processing at the

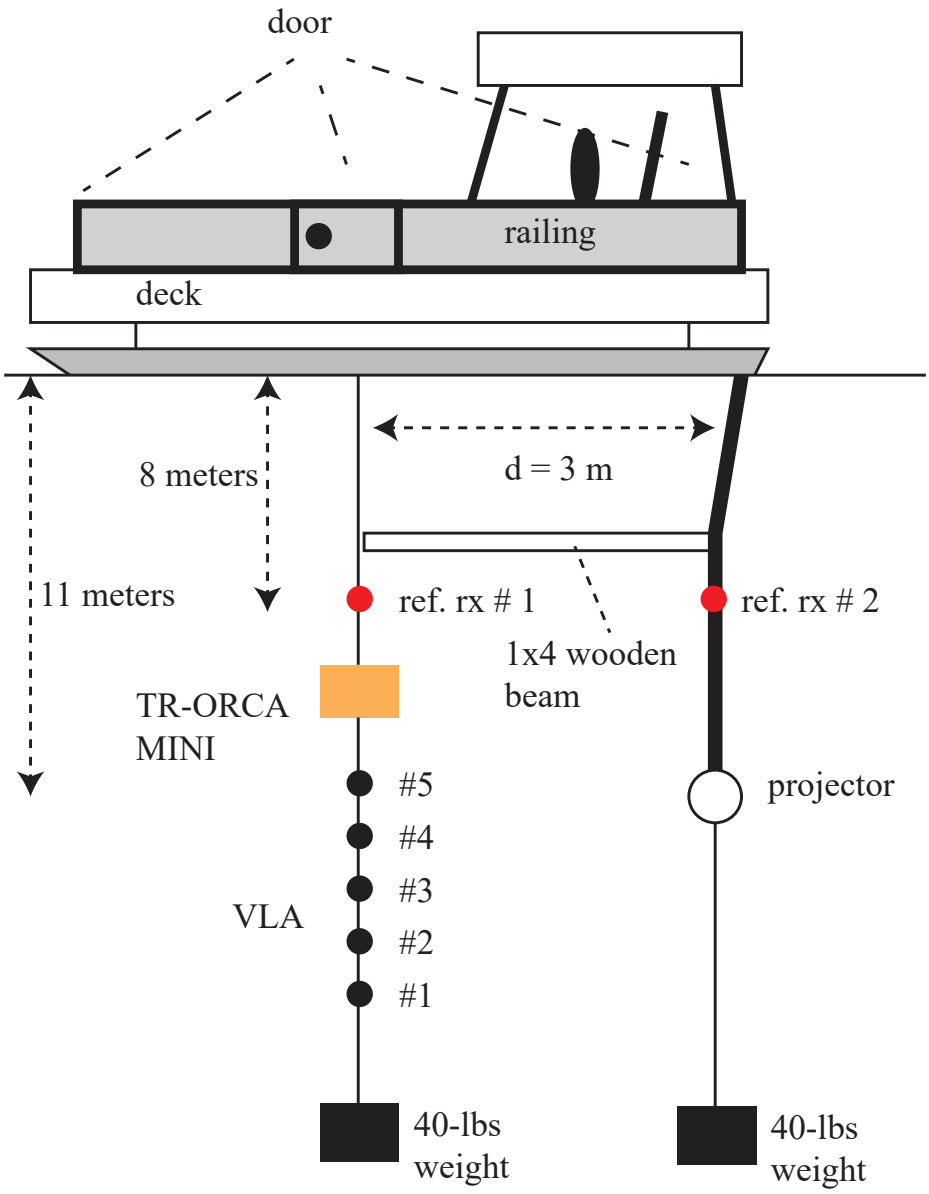

Figure 4.3: Deployment of the equipment below the pontoon deck.

different receivers. The procedure consists in first finding the sound pressure level at the receiver using the data saved in the wavefile. The data saved in the wavefile is converted to the RMS voltage level using the analog-to-digital scaling factor. For the Turbulent Research (TR) VLA hydrophones, the ADC full scale corresponds to 1.8 V, while for the Benthowave reference hydrophones, the full scale corresponds to 3.125 V. Then, for a given hydrophone sensitivity, the receiver sound pressure level is:

$$SPL_r = 20\log_{10}(V_{RMS}) - S. \tag{4.2}$$

The TR hydrophone sensitivity is calibrated to be $S = -165$ dBV re 1μPa, while the Benthowave sensitivity, is $S = -199$ dBV re 1μPa. Then the SPL is evaluated at 1 meter from the source, using spherical spreading and accounting for the distance between the transmitter and receiver, $\mathrm{SPL_t}$. Finally, for a given measured transmit voltage V_{TX}, the transmit voltage response (TVR) is evaluated using:

$$TVR = SPL_t - 20\log_{10}(V_{TX}). \tag{4.3}$$

4.2.1 Reference Hydrophone #1

The reference hydrophone #1 was attached to the receive array approximately 8 m below the sea surface. The horizontal distance between the projector and receiver is 3 meters, controlled by the wood beam. The projector TVR measured using the reference hydrophone #1 supplied by Benthowave is extracted and shown in Figure 4.4.

Note that for all measurements taken, when the transmit voltage is at its minimum of 20 V_{RMS}, the TVR appears higher than for all other voltage settings. This is attributed to a measurement error at the transmitter at low transmit voltage. Also, at 630 V_{RMS}, the signal is clearly saturated at the operating frequency. As can be observed for standard voltage settings between 32-204 V_{RMS}, the TVR at the 2048 kHz operating frequency is 134 dB re 1 μPa/V at 1 m. The 3-dB bandwidth is between 1850 and 2100 Hz, for a total bandwidth of 250 Hz. In comparison, the 3-dB

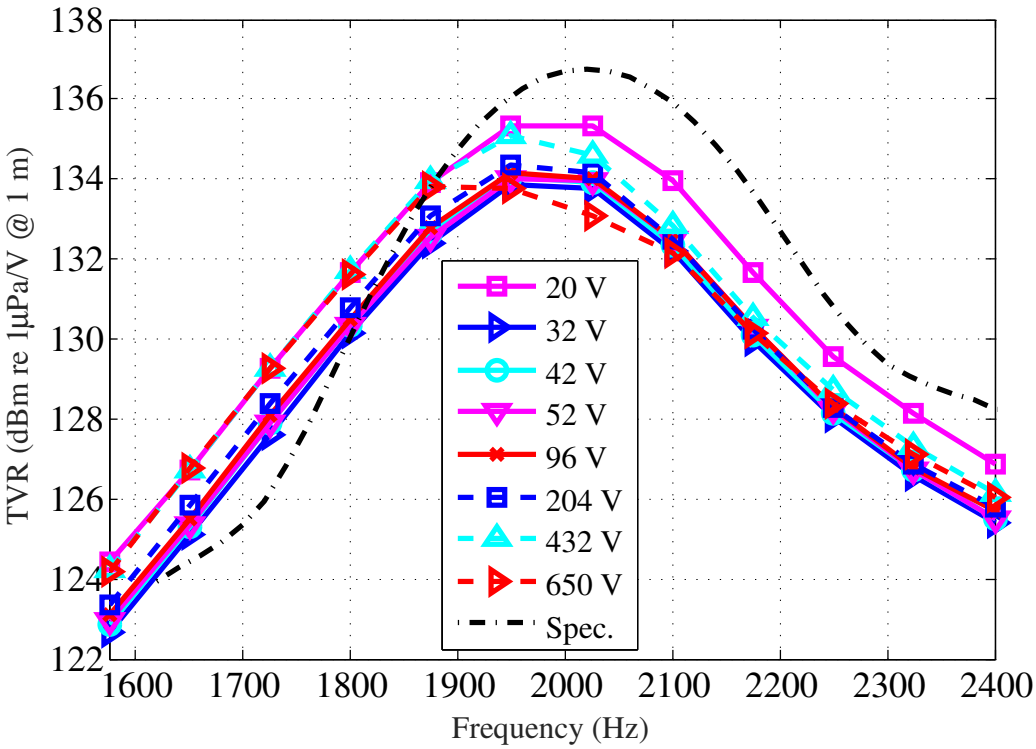

Figure 4.4: Projector TVR measured using hydrophone #1.

bandwidth specification provided is 300 Hz, between 1880 and 2180 Hz. As shown in Fig. 4.4, the TVR is slightly lower, and the bandwidth is also smaller than the provided specification.

4.2.2 Vertical Line Array

Next, the TVR is evaluated using the vertical line array. In Figure 4.5, the TVR measured at all five hydrophones, for a transmit voltage of 32-VRMS is shown. This voltage was chosen to avoid saturation of the VLA. At the resonance frequency there is a variation in the TVR of 3 dB across the five hydrophones. Off resonance, the variation is much lower. The bandwidth of the system is equal to 300 Hz, between 1875 and 2175 Hz. The received hydrophone #3 measured a different response. This may be attributed to a shading effect. The shading can be due to the wood beam or due to the rubber mount that attaches the hydrophone to the tether.

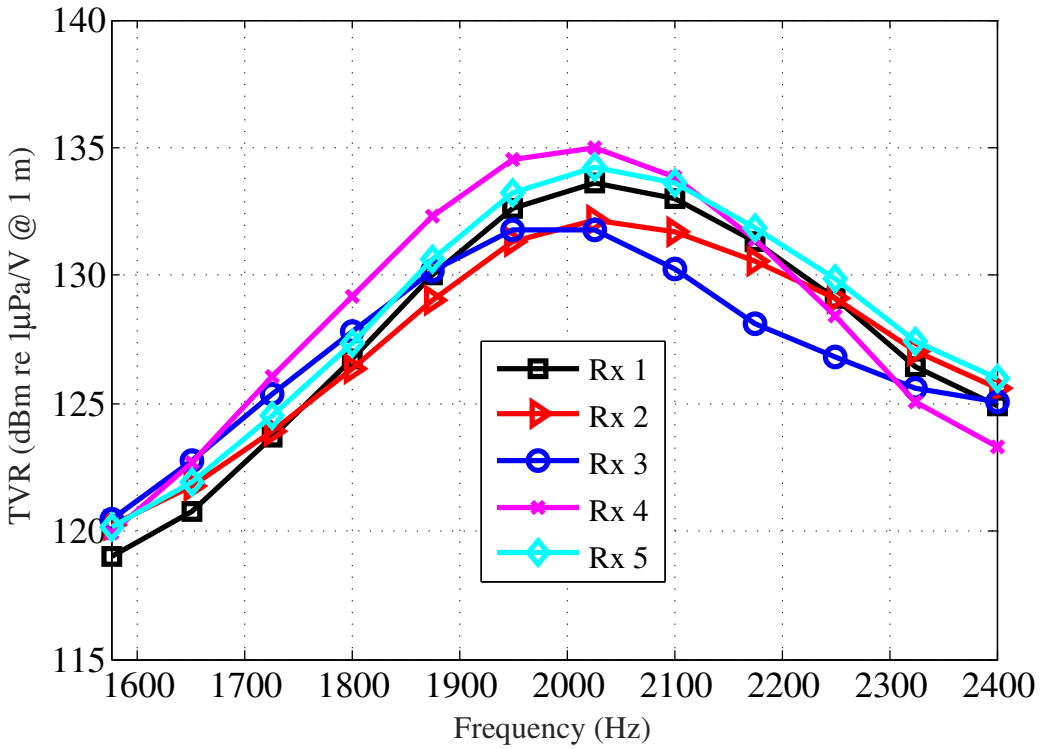

Figure 4.5: Projector TVR measured using VLA at 32 V_{RMS}.

4.2.3 Acoustic Propagation Model

In this Section, measurement results taken during the pre-trial are used to predict the channel transmission loss, and delay spread. Using these results, the waveforms for the final trial were chosen.

The sound speed profile (SSP) of the area can help define an optimal deployment height for the transmitter and receiver. If the SSP varies with depth, the acoustic signal refracts as it propagates and the refraction can be simulated using a ray model such as Bellhop. Because of refraction, the signal may behave as though it were propagating through a waveguide and an optimal receiver placement strategy can be defined. To provide an estimate of the SSP, a hand-held CTD from CastAwayCTD was casted several times throughout the day during a pre-trial held on July 19 at the geographical location of the receiver location. The hourly SSPs are shown in Figure 4.6.

Three CTD casts were carried out near the receiver's location at different times during the experiment. Overall, the sound speed profile remained fairly constant over the span of the deployment. The thermocline extends down to 15 m and the temperature is approximately $4 \deg C$ afterwards.

A sound speed profile was taken during the sea trial and used to run a bellhop simulation that generated the results presented in Figure 4.7. The Figure shows the transmission loss using Thorp's attenuation as a function of range and depth. When the source is placed at 21 m deep, a strong direct path is noticeable and the transmission loss, as a function of range, is slightly lower than when the source is at 35 m deep. This is possibly due to the downward refracting nature of the sound speed profile advantaging the shallower source placement.

If the sound speed profile chosen for the simulation above is representative of the environment in which the sea trial will be occurring, the following considerations should be taken:

- A shallower projector yields higher energy levels at the receiver;

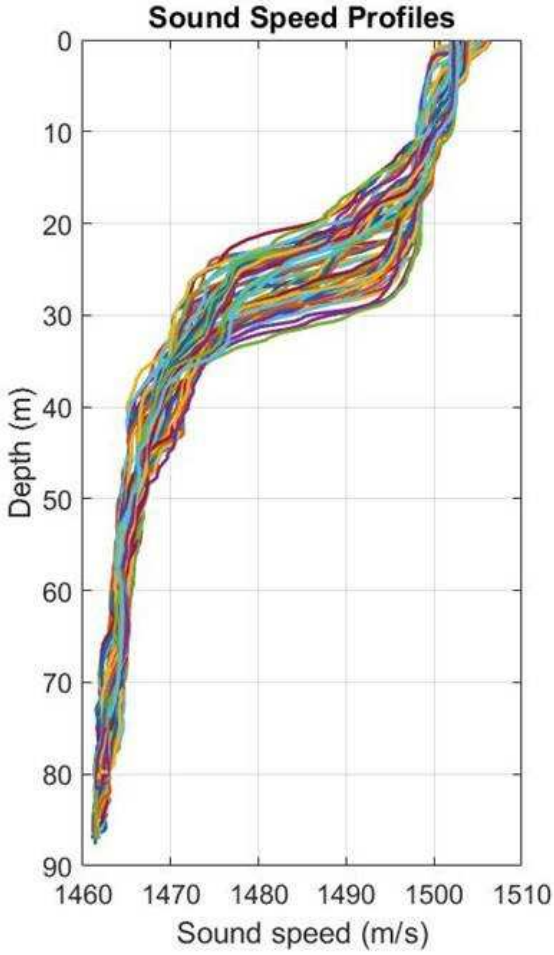

Figure 4.6: Hourly SSPs measured by a CTD [Miron-Morin]

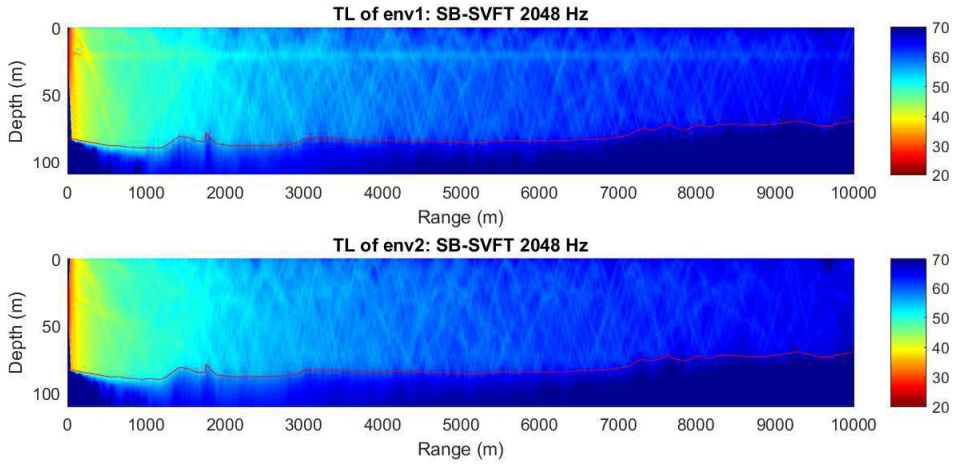

Figure 4.7: Transmission loss for source at a) 21m b) 35m deep. [Miron-Morin]

- A deeper projector yields a smaller delay spread; and
- The placement of the receiver within the water column has significant impact on delay spread, however matching the projector's depth allows for better received signal strength.

4.3 Sea Trial

The location for the sea trial is near St-Margaret's Bay, approximately 10 km from shore. The approximate location for the receiver is at (44.405, -63.825) in a maximum water depth of 100 meters. In Figure 4.8, the approximate GPS location for the receiver and transmitter locations is overlaid over the bathymetry information obtained from the Canadian Hydrographic Services at DFO.

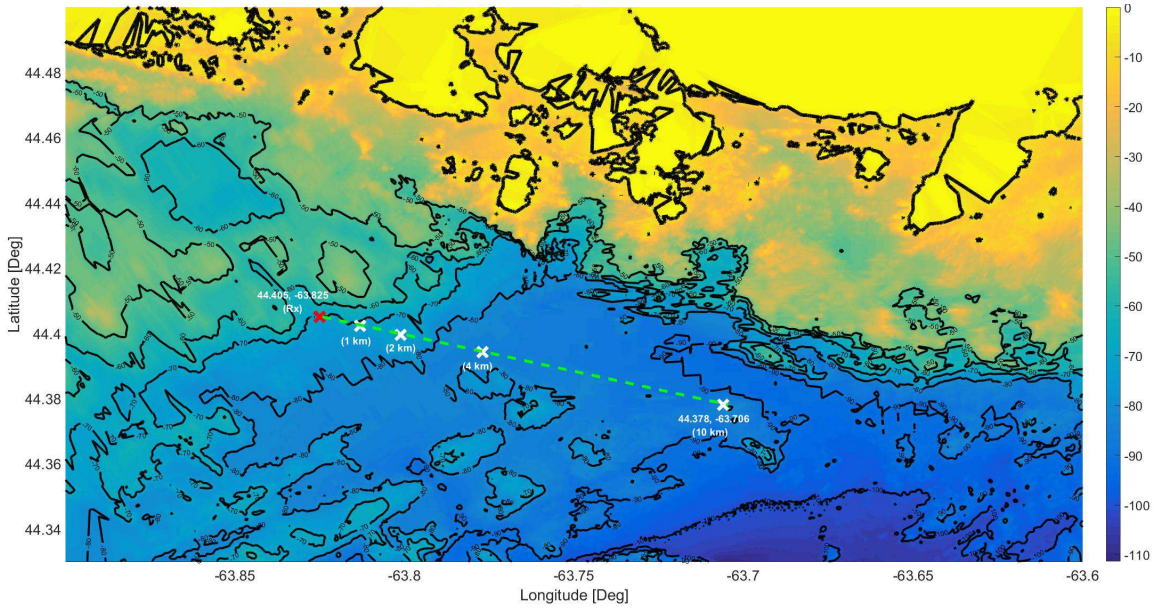

Figure 4.8: Bathymetry Contour Map with Sea Trial Location

4.3.1 Deployment Procedure

In this Section, the deployment procedure in St-Margaret's Bay will be described.

The sea trial is coordinated with the help of Luna Ocean Consulting, Inc. Luna Ocean Consulting owns facilities in the area.

The vessel utilized is the Saorsa, a Northumberland hull Cape Islander, 12 m long, 3.7 m wide (40 ft by 12 ft) with a small enclosed wheel house, Figure 4.9. A 2000 W 120 V generator provided by Luna is used to drive the power amplifier, and for support equipment. GPS locations during the deployment are monitored by the boat captain. A hoist installed on the Luna is also used during deployment and recovery of equipment.

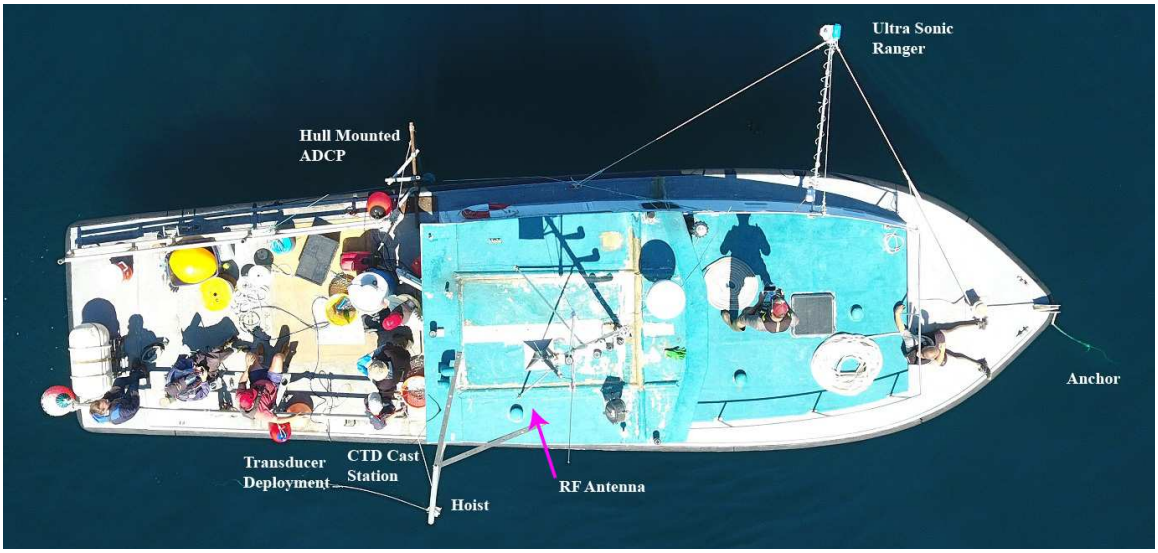

Figure 4.9: Overhead picture of the Saorsa with geared deployed on first day of the trials

For safety issues, and quality of measurements, operations is limited to about sea-state 2.5 and winds less than 15 knots. On day #1, the winds are very low, below 10 kph and the sea state consist solely of a swell, while on days #2 and #3, the winds are approximately 16-24 kph, with the most gusty day being on day #3. The sea state on days 2 and 3 are estimated to be between 2 and 2.5.

A cross-section of the deployment is shown in Figure 4.10 with representative dimensions. Two fixed receivers are co-located, approximately 200 meters apart. Each are anchored to the seabed and separated from one another by approximately 100-200 m to prevent entanglement. The primary acoustic receiver consists of a TR-ORCA with a five-hydrophone vertical line array (VLA). The VLA inter-element spacing is

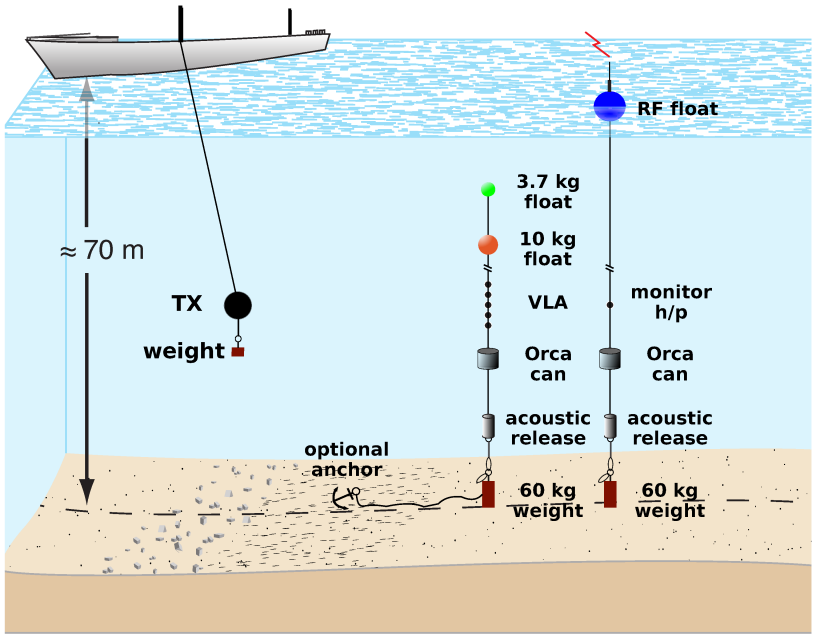

Figure 4.10: Depiction of sea trial deployment [P. Hines]

36.6 cm, approximately $\lambda/2$ at the centre frequency of the acoustic operating band. The VLA depth is positioned to be approximately in the middle of the water column at 35 meters. It is anchored to the seabed using an acoustic release and during the final trial it has no surface expression. The VLA depth is recorded over the two days. The output of the loggers is shown in Figure 4.11 during two days of the deployment. For the receiver, the depth is referred to the top most hydrophone (#1). The periodic change in water depth is attributed to tides in the area. The receiver distance from the seabed remained very stable throughout the experiments. For the transmitter, the values shown include a 1.42 meter offset between the depth sensor and the middle of the transducer. As can be observed, the transmitter depth logs are noisy, because the vessel is sensitive to pitch and roll.

To test the communication link at different ranges, the boat was anchored at pre-defined GPS locations and the transmitter was deployed from the vessel. The GPS positions recorded during the trial are reported in Table 4.2. A 16-kg weight was tethered to the transducer during the static deployments. As can be observed in Fig.4.11, the transmitter was deployed for each range at two different depths: the first was chosen to be below the SSP thermocline, a second was approximately in the

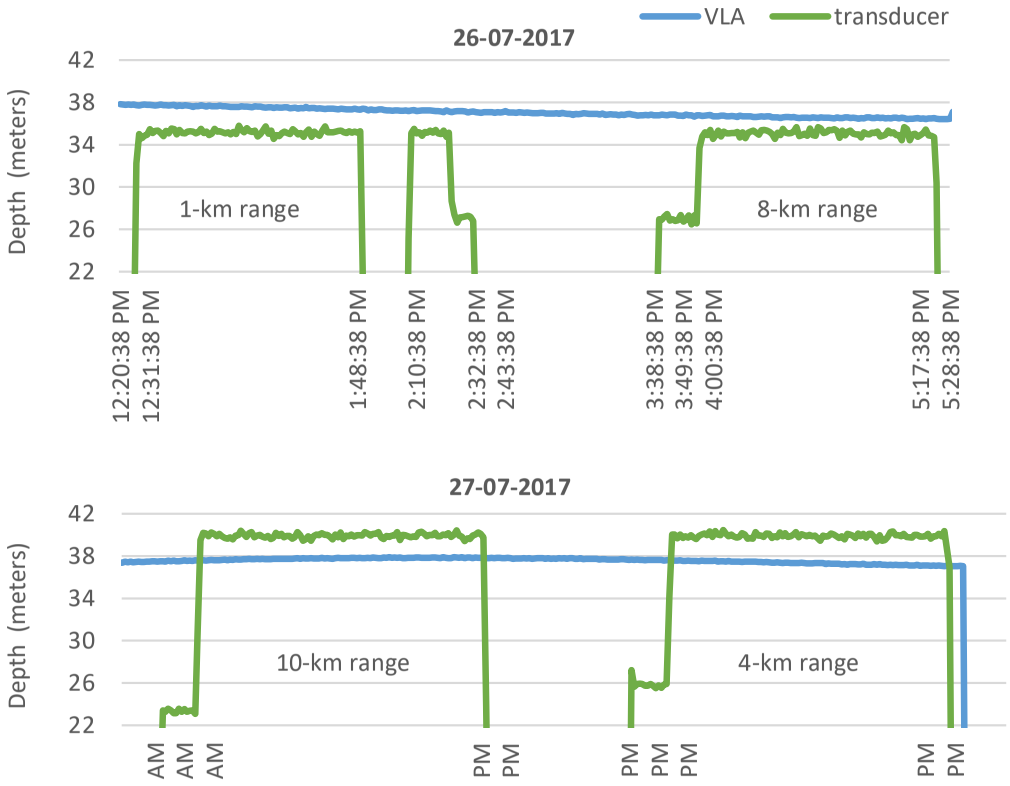

Figure 4.11: Depth logger recorded outputs.

middle of the thermocline. While it is expected that the acoustic propagation will result in lower SPL below the thermocline, a subset of channel sounding measurements are done to confirm this.

Table 4.2: GPS position for the different deployment locations

VLA mooring	N 44°24.166′, W 63°49.257′	day 1& 2
VLA mooring	N 44°24.174′, W 63°49.284′	day 3
Transmitter @ 0.5 km (long sequences)	N 44°24.144′, W 63°48.87′	day 1 AM
Transmitter @ 1 km (short sequences)	N 44°24.144′, W 63°48.522′	day 1 AM
Transmitter @ 2 km	N 44°24.083′, W 63°47.893′	day 3 PM
Transmitter @ 4 km (day 2)	N 44°23.615′, W 63°46.338′	day 2 PM
Transmitter @ 4 km (day 3)	N 44°23.503′, W 63°46.401′	day 3 AM
Transmitter @ 8 km	N 44°23.520′, W 63°43.666′	day 1 PM
Transmitter @ 10 km	N 44°23.315′, W 63°42.089′	day 2 AM

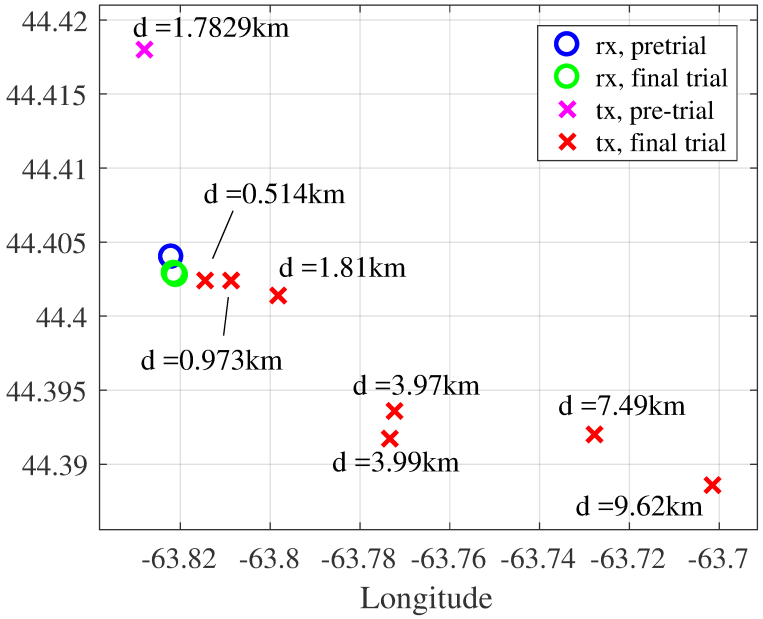

Figure 4.12: Recorded Latitude/Longitude Position of the Equipment

To supply the signal, the transmitter electronics and power amplifier are installed inside the wheel house on the co-pilot station. For each range, a set of pre-defined waveforms are loaded and played using Matlab. The output is fed to the power amplifier through the internal sound card. In the final trial a Hammond transformer with a turns ratio slightly above five is used to increase the output RMS voltage well

above 630 V_{RMS}. Note that the output voltage is monitored using a multi-meter. To maintain safe operation, the high power electronics are housed inside a toolbox, with proper connectors supplied by the Electrical Engineering Department.

Physical oceanography conditions were monitored using a CTD, an ultra sonic sensor as well as an acoustic Doppler current profiler (ADCP). As well as measuring the local currents, the ADCP provided an estimate of surface wave height. The ADCP is mounted on the vessel to obtain a transect.

4.3.2 Experiments

The specific objectives of the proposed sea trial are 1) to characterize the propagation channel for medium to long range underwater acoustic communication in a point-to-point link and correlate it with oceanographic conditions, and 2) confirm the reliability of novel underwater acoustic communication techniques.

To transmit the communication waveforms, wavefiles were generated and saved in a database. The files were played using the transmit laptop soundfile, amplified to the appropriate level, and applied to the transmit sound source. Each wavefile was played for each deployment setup. They are listed in Table 4.3.

Table 4.3: Description of FSK files to be transmitted

Filename	Description	Duration (min)
wavefile1.wav	Channel Sounding, LFM [Bousquet]	10:00 min
wavefile5a.wav	16-Parallel BFSK turbo coded	10:00 min
wavefile5b.wav	32-FSK turbo coded	10:00 min

Prior to each test, the transmit power will be adjusted to ensure a respectable in-band SNR at the receiver. For this purpose, a transmit reference will be sent and the received signal will be measured until the received signal has the appropriate power.

Measurements will be made at distances between 1 km and 10 km. Nominal distances of 1, 2, 4, and 10 km have been identified to quantify the degradation of the acoustic signal as a function of range. At the maximum voltage setting, the output power is 144 W. Since the power amplifier is running at relatively low efficiency, a

2000 W generator is used to provide sufficient energy for the duration of the experiments.

The pair of experiments that will be analyzed in this work to assess the performance of the communication system are characterization of the time-variant underwater acoustic channel properties and evaluation of a highly reliable non-coherent encoded modulation technique. Additionally, the noise power will be assessed.

4.3.2.1 Noise Analysis

To characterize the performance of the communication system, it is important to assess the ambient noise conditions during the deployment. For this purpose, the noise PSD, and pressure level are measured. Note that throughout the experiments the sampling rate was fixed at 24 ksps. The ADC scaling is defined such that the maximum value (+1) represents an instantaneous voltage of 1.5 V. As can be observed, a different DC offset is present at the output of each channel, and should be compensated before post-processing. There is also a clock frequency offset ratio equal to 1.0006 in the TR-ORCA that must be compensated by resampling the input signal.

Prior to each experiment, a 10 minute sequence of noise is analyzed. The PSD is evaluated using the `pwelch` function in Matlab. The output $N(f)$ of the `pwelch` function is converted to dBm re 1 μPa using

$$PSD = 10\log_{10}(1.5^2 N(f)) + 165 \tag{4.4}$$

The noise sound pressure level (SPL) is also calculated by averaging over 1 second windows. Its value is evaluated before and after the bandlimiting filter used in the communication digital post-processing. As expected, the SPL is lower on day 1, when the sea was calm, while day 2 and day 3 present increased noise levels. For a digital signal $n(t)$ produced by the recorder, the SPL is obtained using

$$SPL = 20\log_{10}1.5 \times n(t) + 165 \tag{4.5}$$

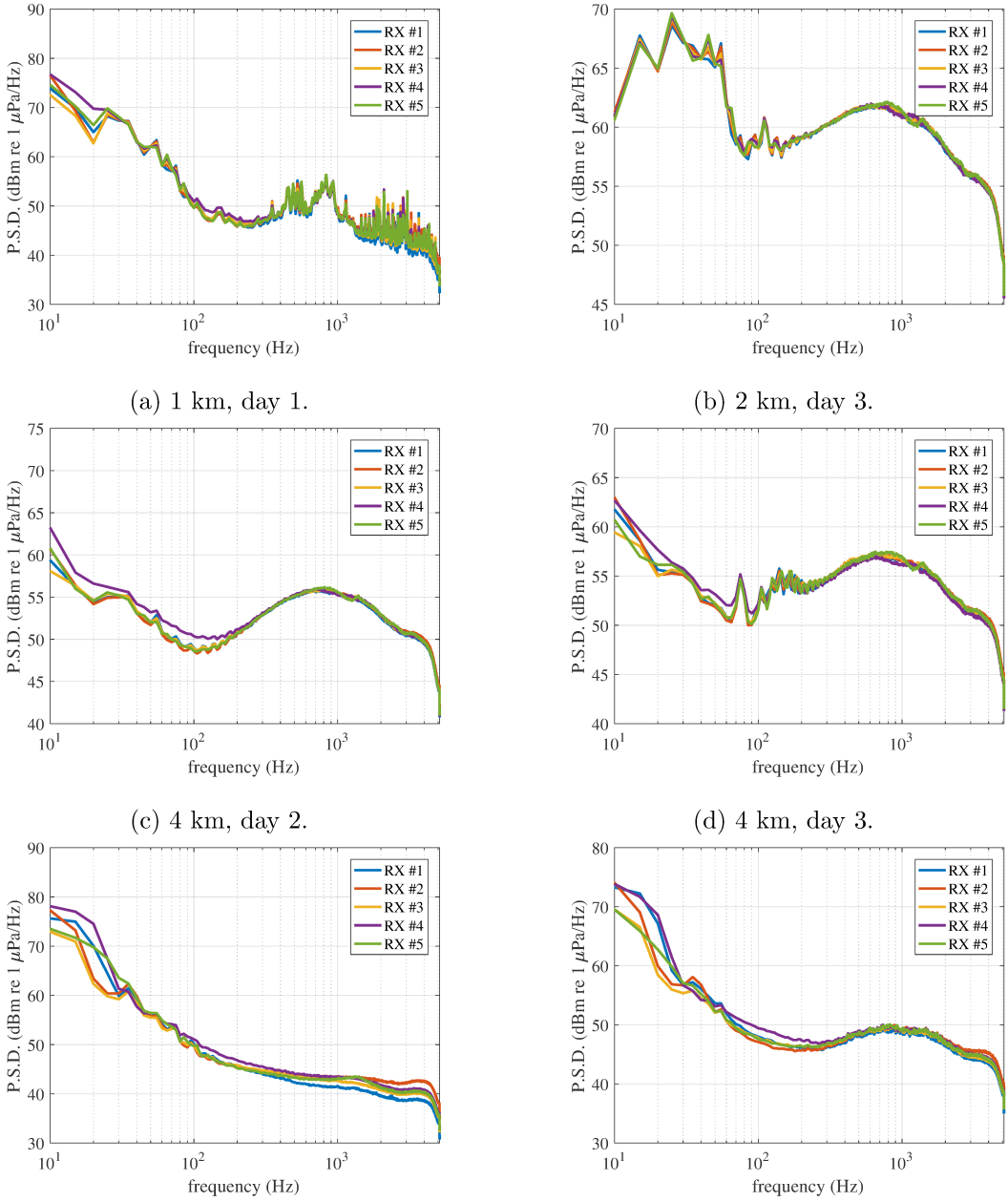

(a) 1 km, day 1.

(b) 2 km, day 3.

(c) 4 km, day 2.

(d) 4 km, day 3.

(e) 8 km, day 1.

(f) 10 km, day 2.

Figure 4.13: Noise P.S.D. prior to each range test.

The average noise SPL over the complete recorder bandwidth is measured for each hydrophone output. The average noise power is evaluated at the output of the receiver matched filter, shown in Table 4.4. A mean value averaged over all the hydrophone outputs is also reported. This will allow the estimation of the received signal to noise ratio during the experiments.

Table 4.4: Average noise SPL at output of matched filter for each deployment range.

	RX #1	RX #2	RX #3	RX #4	RX #5	E[·]
1 km, day 1	66.25	66.84	66.56	66.52	66.78	66.59
2 km, day 3	78.39	78.58	78.51	78.45	78.67	78.52
4 km, day 2	72.77	72.90	72.85	72.81	72.98	72.86
4 km, day 3	73.91	74.05	74.03	73.65	74.17	73.96
8 km, day 1	58.73	60.90	60.02	60.76	59.95	60.07
10 km, day 2	65.99	66.52	66.30	66.48	66.49	66.36

4.3.2.2 Channel Characterization

The objective of this experiment is to evaluate the channel impulse response as a function of time.

Note that to quantify the propagation properties, the transmit power as well as the exact start time of each frame will be recorded on the transmit laptop. Ideally, the time stamp will be recorded with a resolution on the order of a few μseconds. A chirp sequence is transmitted to characterize the channel in the presence of Doppler. The data is recorded at 24 ksps. The output of the recorder is resampled at 10.24 ksps and the resampling operating also includes an additional factor of 1.0006 (5003/5000) to compensate for the inherent clock drift in the recorder. After post-processing, the CIR was obtained using an LFM is shown in Figure 4.14. Note that the CIR is shown for the different measurement ranges, but only for the output of the hydrophone #1, and the output of the other hydrophones have similar long-term characteristics.

A close observation of the CIRs shows that for ranges at 2 km and 4 km, that the channel delay is variable. During these two trials the sea state was relatively high between 2 and 2.5, and even if the vessel was anchored, it was drifting through the experiments. It can also be observed that as the distance between the transmitter

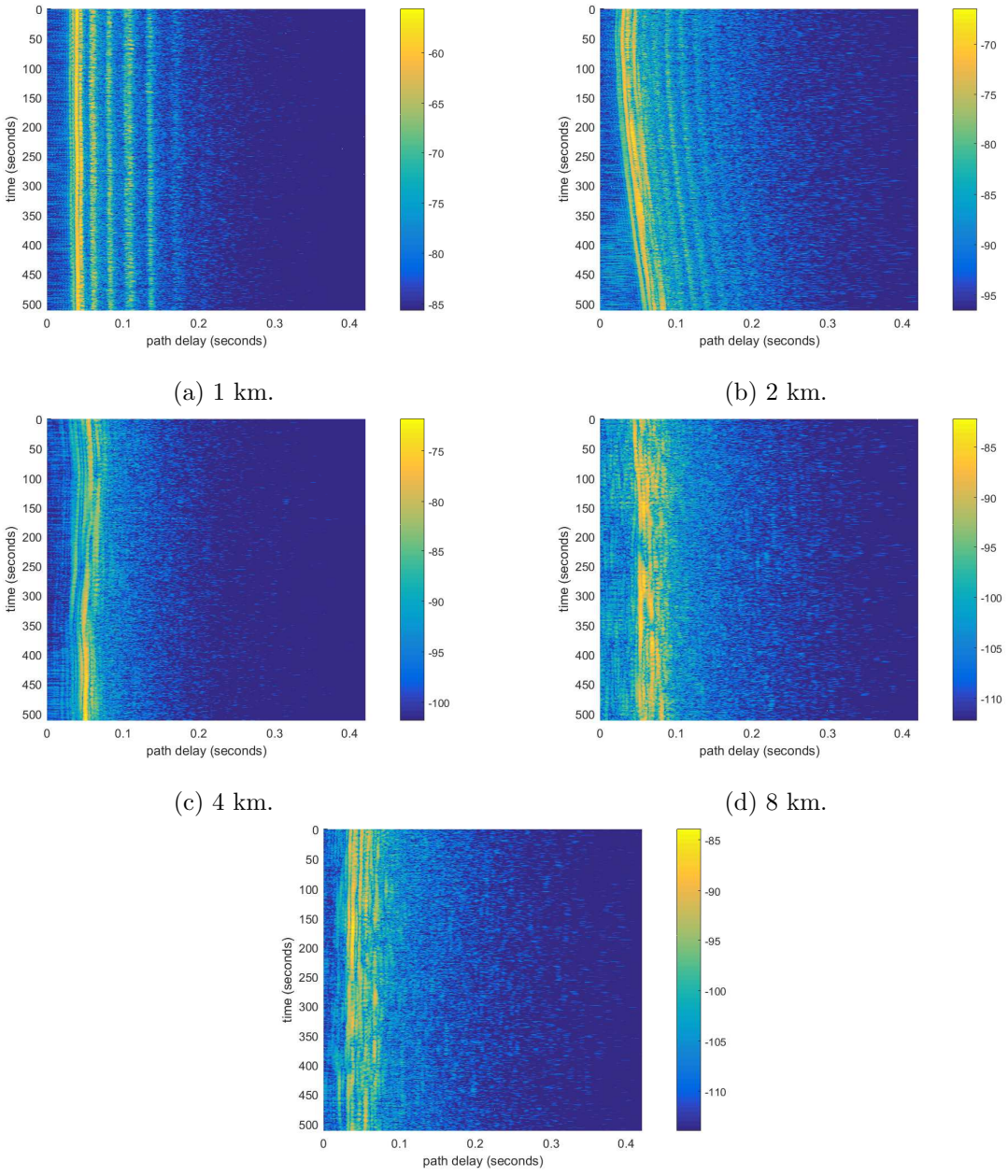

(a) 1 km.

(b) 2 km.

(c) 4 km.

(d) 8 km.

(e) 10 km.

Figure 4.14: Channel impulse response in dB as a function of time measured using LFM on hydrophone #1.

and receiver increases, the multipath echo arrival becomes more diffuse while the significant path arrival delay is more spread.

In Figure 4.15, the average of the channel frequency response is shown. This Figure shows the frequency selectivity of the channel for each hydrophone at each of the transmission distances. For example, as shown in Figure 4.15c, hydrophone #5 experiences a deep fade in signal energy. During deep fades, signal energy drops significantly and this can cause reception errors in a communication system. The implementation of turbo code corrects these type of signal errors through interleaving and redundancy.

The average Doppler spread of the channel is measured for each distance, shown in Figure 4.16. Due to the relatively calm sea state and weather conditions during the sea trial, the affect of Doppler spread is negligible and well within the 10 Hz frequency separation.

The multipath delay spread is measured as a function of time for all ranges, shown in Figure 4.17. The maximum recorded RMS delay spread is approximately 0.08 seconds, a value representative of the Bellhop model in Section 2.5.

To further analyze the CIR, a single channel profile is represented in Figure 4.18 for the LFM.

4.3.3 FSK Results

This section discusses the post-processed results from the non-coherent waveform transmissions during the sea trial and are outlined in [22].

Following the experiments, the data was post-processed. This was accomplished using the free, open source, digital audio editor known as Audacity. Shown in Figure 4.19 is a sample of 1 recorded channel represented on a spectrograph. Following a series of incrementally increasing frequency pulses are the 10 minute long wavefiles. The individual wavefiles were extracted visually from Audacity. Figure 4.20 shows the end and start of two sequential waveforms. It can be seen from the Figure that there are multipath echoes following the end of transmission. A short wait period

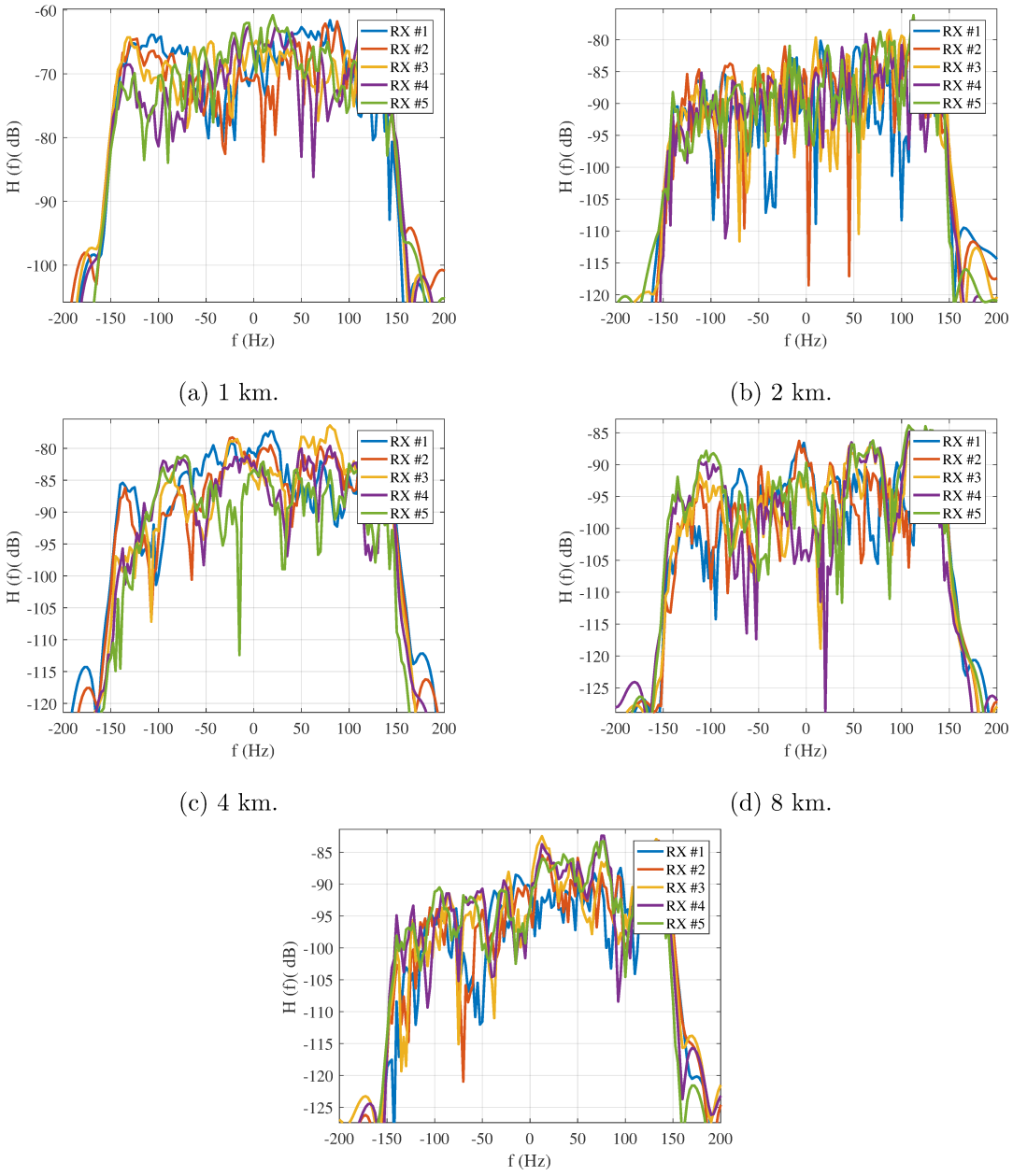

(a) 1 km.

(b) 2 km.

(c) 4 km.

(d) 8 km.

(e) 10 km.

Figure 4.15: Average of the channel frequency response using LFM

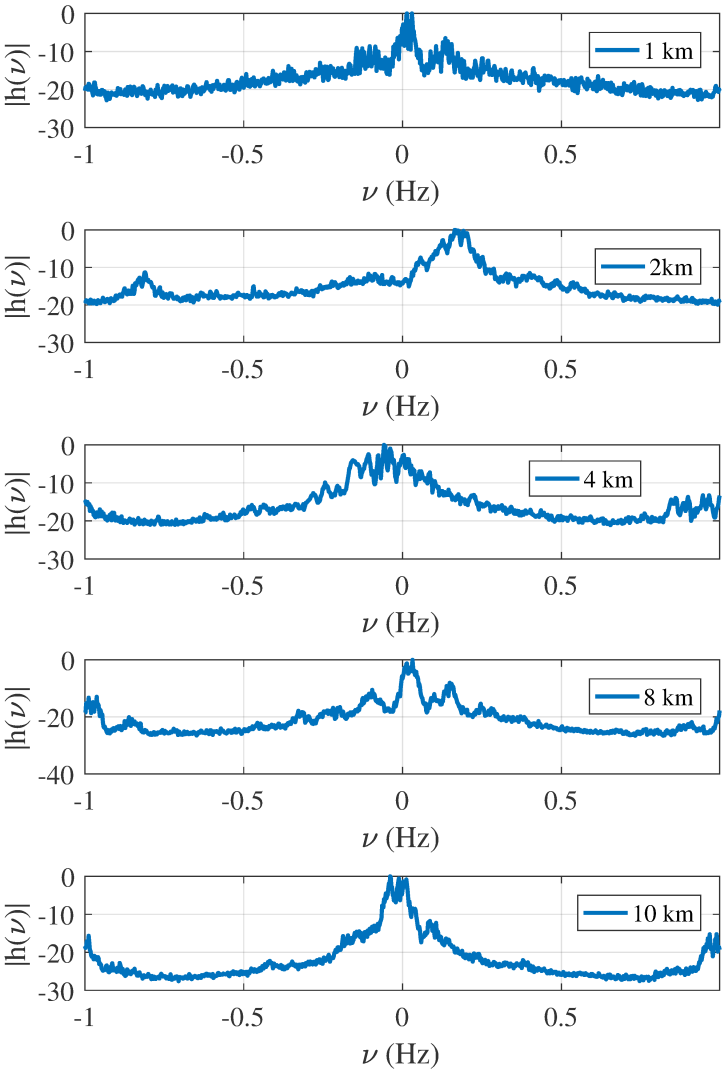

Figure 4.16: Doppler spread for all ranges represented in dB

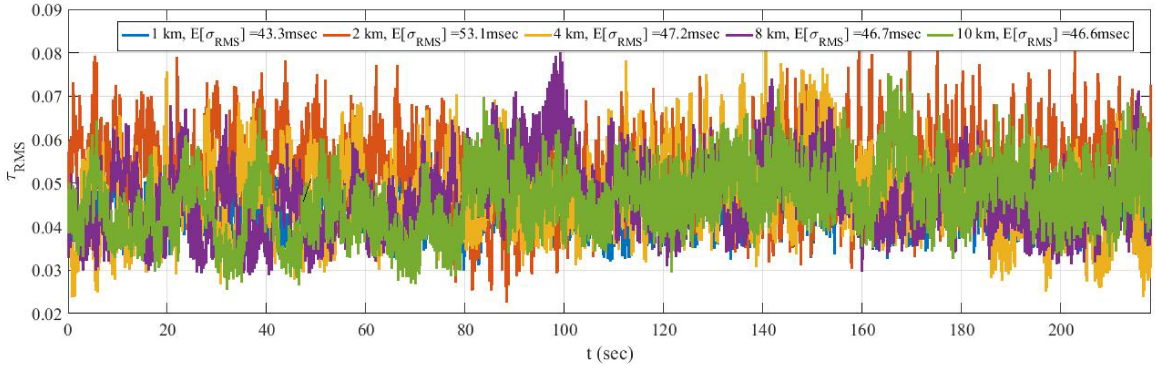

Figure 4.17: Delay spread as a function of time for all ranges

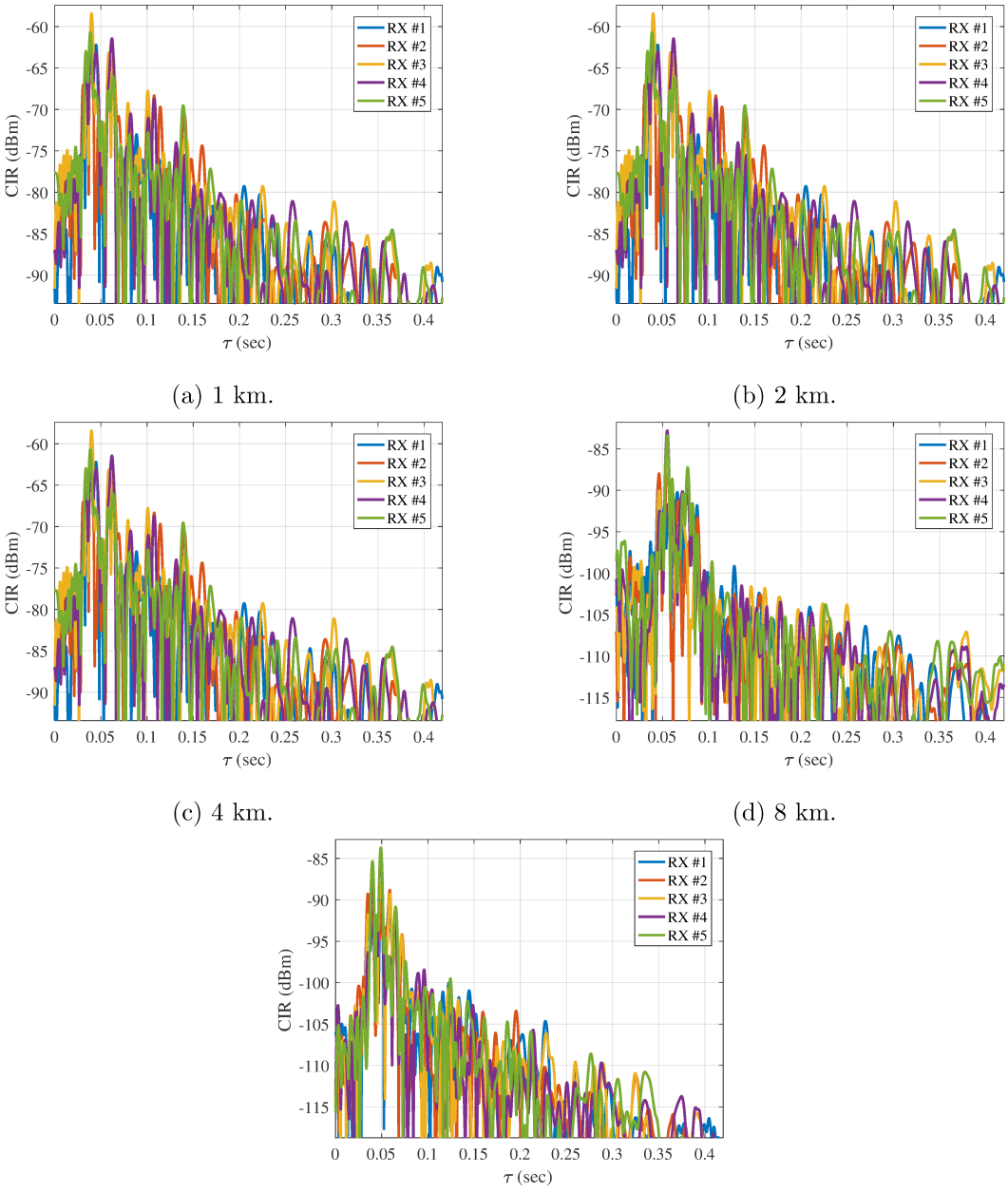

(a) 1 km.

(b) 2 km.

(c) 4 km.

(d) 8 km.

(e) 10 km.

Figure 4.18: Example of channel impulse response (# 74) in dB measured using LFM.

ensured the echoes were negligible before the next transmission. To assist in proper extraction of the received wavefile, audio cues can also be heard to realize the end of transmission.

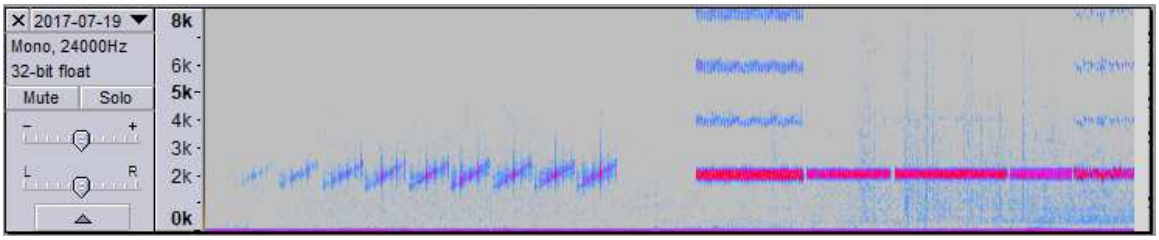

Figure 4.19: Sample Audacity screenshot

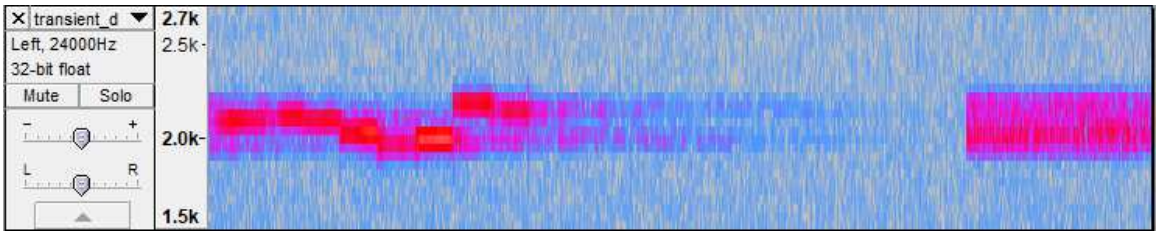

Figure 4.20: Audacity screenshot showing transmission end and start (8km distance)

It was found through observation on every wavefile that was isolated that the duration of the received waveform was not exactly 10 minutes long. To be more precise the difference in time between the start and stop time should be exactly 600 seconds (10 minutes). This was not the case for the received waveforms and was consistently true. The difference could be due to human error in selecting the start and stop times, Doppler shift and spread dilating or compressing the signal, or sample clock inaccuracies/drift. The duration of each wavefile was approximately 0.3 seconds too short or about 599.7 second total duration. To correct for the compression of the waveforms, they had to be rescaled or uncompressed for proper demodulation. Table 4.5 lists the rescaling factors for each transmission. Disregarding the 8 km transient factor, the difference between factors is nearly negligible. The assumption is that the compression of the signal is consistent throughout the signal.

Following the rescaling of the waveforms, they are now suitable for proper demodulation and decoding. Table 4.6 shows the BER after demodulation without Turbo decoding for 32-FSK for each hydrophone channel. During the first day of sea trials, both algorithms were designed to have a symbol period of 0.5 seconds and were

Distance	32-FSK	16p-BFSK
1 km	1.000547	1.000567
2 km	1.000534	1.000534
4 km	1.000500	1.000550
8 km	1.000400	1.000517
10 km	1.000567	1.000584

Table 4.5: Waveform Re-scaling Factors

transmitted at 1 and 8 km. The purpose of the symbol time of 0.5 seconds allows the analysis of symbol length on performance. For the following two days, the symbol period was adjusted to 1 second for 2, 4, and 10 km distances. This is evident in the number of bits transmitted. To summarize the daily transmissions: Day 1 sent 1 km and 8 km with symbol time of 0.5 seconds, Day 2 sent 4 km and 10 km with symbol time of 1 second, and Day 3 sent 2 km and 4 km (16-BFSK only). The BER results for non-Turbo 16-BFSK is shown in Table 4.7. The received SNR was measured to be approximately 30 dB.

The bit error ratio measured for 32-FSK with Turbo observed an average BER of 0.00016 and the BER for 16-BFSK with Turbo observed a value of 0. The addition of this channel encoder drastically improved the reliability of the system resulting in minimal to zero errors. Note that even when the symbol period was set equal to 0.5 seconds for the first day, the BER of the Turbo-coded waveforms was equal to zero.

From the bit error ratio tables, one can observe the performance degradation due to a smaller symbol time (1 km and 8km compared to 2 km, 4 km, and 10 km). This degradation occurred because the symbol time of 0.5 seconds is significantly more affected by the multipath delay spread. Another important observation is the difference between 2km, Day 2 and 2km, Day 3 in Table 4.7. The sea state during day 3 was calmer than that of day 2 resulting in less ambient noise and other signal deteriorating effects. As a result of a calmer sea state, the Day 3 results were significantly better than those of Day 2.

Shown in Figure 4.21 is a graphical representation of the average BER results from the sea trial for each algorithm. Two definitive points can be drawn from this figure, 1) that reducing the symbol period increases the number of bit errors, and 2)

Dist.	Ch. 1	Ch. 2	Ch. 3	Ch. 4	Ch. 5	Average	Total Bits
1 km	0.0183	0.0227	0.0182	0.0182	0.0193	0.0193	6000
2 km	0.0177	0.0153	0.0077	0.0087	0.0110	0.0121	3000
4 km	0.0143	0.0223	0.0110	0.0123	0.0230	0.0166	3000
8 km	0.0490	0.0430	0.0430	0.0485	0.0430	0.0453	6000
10 km	0.0243	0.0233	0.0180	0.0197	0.0177	0.0206	3000

Table 4.6: Bit Error Ratio - 32-FSK - No Turbo

Dist.	Ch. 1	Ch. 2	Ch. 3	Ch. 4	Ch. 5	Average	Total Bits
1 km	0.0176	0.0219	0.0193	0.0227	0.0225	0.0208	19200
2 km	0.0127	0.0104	0.0082	0.0085	0.0099	0.0099	9600
4 km, Day 2	0.0157	0.0163	0.0109	0.0140	0.0128	0.0139	9600
4 km, Day 3	0.0064	0.0056	0.0076	0.0115	0.0096	0.0081	9600
8 km	0.0287	0.0282	0.0292	0.0270	0.0249	0.0276	19200
10 km	0.0161	0.0144	0.0156	0.0174	0.0165	0.0160	9600

Table 4.7: Bit Error Ratio - 16-parallel BFSK - No Turbo

degradation in performance correlates with increased communication distance.

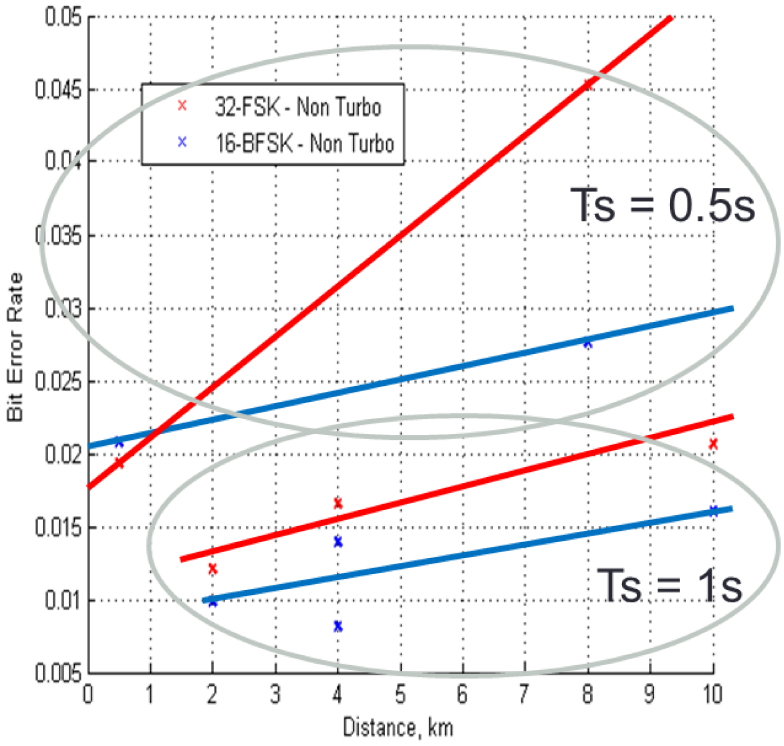

Figure 4.21: Graphical representation of average BER results

Furthermore, a comparison between the sea trial results at 10 km and simulation results can be found in Table 4.8. The received SNR at 10 km during the sea trial was approximately 25 dB. The BER results for the simulation comparisons were taken corresponding to this value. The turbo coded results for simulation are not applicable as the simulations did not obtain BER values for such a high signal energy. This was due to the extensive simulation processing time required to generate BER results at such a high SNR. For the non-turbo coded algorithms, the simulations show comparably identical BER performance as the sea trial.

Encoding	**32-FSK Sim.**	**32-FSK S.T.**	**16-BFSK Sim.**	**16-BFSK S.T.**
Non-turbo	0.030	0.021	0.020	0.016
Turbo	N/A	0	N/A	0

Table 4.8: Sea trial (S.T.) and simulation (Sim.) comparison at 10 km (25 dB SNR)

As a secondary measure to evaluate the performance of these algorithms, euclidian distances between bit decisions were also calculated. This gives a confidence measure for the systems where no bit errors were detected. Since the Turbo and non-Turbo results were extracted from the same received waveform, the euclidian distances for turbo and non-turbo are identical. In the demodulation code, an integration is used for the energy detection in a sub-band. The choice for bit decisions is based upon the maximum value integration corresponding to a specific subcarrier frequency. The euclidian distance is a measure between the maximum value (the decision) and the second highest value. Note that in some instances, due to multipath, Doppler, and high noise levels, the maximum value choice is incorrect. In Table 4.9, the euclidian distance was calculated and shows the maximum, minimum, and mean values for 32-FSK algorithm. Values corresponding to waveform transmissions at 1 km and 8 km were disregarded since these waveforms were generated with T_s equal to 0.5 seconds as opposed to 1 second.

The maximum value infers a strong decision was made, the minimum value is a weak decision, and a high mean infers the confidence for the majority of decisions. Small minimum and mean values are problematic and indicate a greater probability for incorrect bit decisions. This means that at least two sub-frequencies contain nearly equal amounts of energy. The results for the 16-parallel BFSK algorithm are shown

in Table 4.10.

Distance	**Maximum**	**Minimum**	**Mean**
2 km	305.352	0.0434	68.787
4 km	131.688	0.0140	27.682
10 km	43.677	0.0023	10.052

Table 4.9: Euclidian Confidence between Bit Decisions - 32-FSK

Distance	**Maximum**	**Minimum**	**Mean**
2 km	31.5210	0.0004	7.7756
4 km, Day 2	12.468	0.0000	2.617
4 km, Day 3	19.375	0.0002	3.582
10 km	5.577	0.0002	1.057

Table 4.10: Euclidian Confidence between Bit Decisions - 16-parallel BFSK

Comparing the results from Tables 4.9 and 4.10 with the bit error ratio from Tables 4.6 and 4.7, respectively, one confirms the correlation between degradation in confidence with increase in bit errors. It is also shown that with increasing distance, system performance degrades.

Chapter 5

Conclusion

In this work, an underwater acoustic link was designed, analyzed modeled, and then tested in realistic conditions. Two low-data rate waveforms, 32-FSK and 16-parallel BFSK, were implemented to achieve high reliability at mid range distances underwater. The addition of Turbo convolutional encoding greatly increased the robustness of both FSK modulation schemes to usable performances. A highlight of this work, is that the signal processing accomplished at the physical layer is highly compatible with standard JANUS.

In this Chapter, the contributions of this work are provided in Section 5.1 and, lastly, Section 5.2 discusses potential future work.

5.1 Summary of Contributions

The research in this thesis describes a design methodology for non-coherent communication modulation schemes in high interference environments. The specifics of implementing a reliable point-to-point link depend upon the channel environment in question. For shallow waters, or situations with large multipath delay spread, long symbol times as well as more reliable error correcting techniques are required to mitigate channel impairments. High reliability FEC techniques, such as turbo, deliver optimal performances with long strings of data, higher complexity encoding, and numerous decoding iterations. As a result, data rate is sacrificed.

The data rate of the link also depends upon the mobility of the platforms and hardware resource allocation. In this thesis, the projector used during the sea trials limited the carrier frequency and bandwidth and realized the application for low-data rate, long distance communication. Higher data rate and more Doppler resistive

modulation designs can be obtained with access to greater bandwidth resources.

In this thesis, two specific non-coherent algorithms were designed for a specific littoral underwater environment 10 km off the coast of Nova Scotia providing a 10 km long, 80 m deep, communication channel. The 16-parallel BFSK was implemented as a bridge between the tonal FSK modulation and OFDM, to provide higher data rates than FSK but maintaining signal processing simplicity.

Specifically, when non-coded, the performance of the 32-FSK and 16-BFSK waveforms achieve throughputs of 5 bps and 16 bps with average BER of 0.0206 and 0.0160 at 10 km, respectively. During day 1 of the sea trial, when the symbol time was set equal to 0.5 seconds, the performance obtained was 10 bps and 32 bps for an average BER of 0.0453 and 0.0276 at 8 km, respectively. The Turbo-coded 32-FSK and 16-BFSK waveforms achieved throughputs of 1.67 bps and 5.33 bps, respectively, while both averaged BERs of zero. The 0.5 second symbol time transmissions obtained performances of 3.33 bps and 10.67 bps at 8 km, also while obtaining zero bit errors.

The quantification of the results with Turbo code are limited due to the insufficient number of bits transmitted. To explicitly quantify the performance measure of the Turbo-coded waveforms, more bits need to be transmitted.

5.2 Future Research

From the observations made during the sea trial, more allocated time is necessary to achieve higher confidence in system performance. To reliably evaluate the performance of the sea trial, more transmission time is necessary to obtain an acceptable number of symbol transmissions. The consequence of low-data rate systems is the time required to receive an acceptable number of symbols.

The future research of this work includes applying the proposed modulation schemes to JANUS. For example, the use of turbo code over the 1/2 rate viterbi encoder may improve robustness, which is important for priority messages. The implementation of a multi-user network using the described modulation techniques would have to be

realized, simulated, and tested. A sea trial procedure for a network deployment is drastically more involved than a point-to-point link deployment.

Other future research directions include a further study of Turbo code, such as implementing higher complexity encoders, studying performance on specific length packets, use of code puncturing to increase throughput, and decidedly choosing the number of decoding iterations to maximize decoder efficiency and performance. The study of utilizing spatial diversity to increase received SNR, this is useful in situations where signal transmit power is limited. Incorporating frame packet design to mitigate channel impairments, such as a guard interval, may also be studied.

Bibliography

[1] F. Campagnaro, R. Francescon, P. Casari, R. Diamant, and M. Zorzi, "Multimodal underwater networks: Recent advances and a look ahead," *WUWNET'17, November 6–8, 2017, Halifax, NS, Canada*, pp. 1–8, 11 2017.

[2] I. F. Akyildiz, D. Pompili, and T. Melodia, "Underwater acoustic sensor networks: research challenges," *Ad Hoc Networks*, vol. 3, no. 3, pp. 257 – 279, 2005.

[3] R. J. Urich, *Principles of Underwater Sound*, vol. 1. McGraw Hill Book Company, 1975.

[4] L. Berkhovskikh and Y. Lysanov, *Fundamentals of Ocean Acoustics*. Springer, 1982.

[5] W. D. Wilson, "Speed of sound in sea water as a function of temperature, pressure, and salinity," *The Journal of the Acoustical Society of America*, vol. 32, no. 6, pp. 641–644, 1960.

[6] C. C. Leroy, "Development of simple equations for accurate and more realistic calculation of the speed of sound in seawater," *The Journal of the Acoustical Society of America*, vol. 46, no. 1B, pp. 216–226, 1969.

[7] D. Tse and P. Viswanath, *Fundamentals of Wireless Communication*. Cambridge University Press, 2005.

[8] A. A. M. Saleh and R. Valenzuela, "A statistical model for indoor multipath propagation," *IEEE Journal on Selected Areas in Communications*, vol. 5, pp. 128–137, February 1987.

[9] P. Qarabaqi and M. Stojanovic, "Statistical characterization and computationally efficient modeling of a class of underwater acoustic communication channels," *IEEE Journal of Oceanic Engineering*, vol. 38, pp. 701–717, Oct 2013.

[10] T. Melodia, H. Kulhandjian, L. Kuo, and E. Demirors, *Advances in Underwater Acoustic Networking*, ch. 23, pp. 804–852. Wiley-Blackwell, 2013.

[11] J. Catipovic, A. Baggeroer, K. V. D. Heydt, and D. Koelsch, "Design and performance analysis of a digital acoustic telemetry system for the short range underwater channel," *IEEE Journal of Oceanic Engineering*, vol. 9, pp. 242–252, Oct 1984.

[12] L. E. Freitag, J. S. Merriam, D. E. Frye, and J. A. Catipovic, "A long-term deep-water acoustic telemetry experiment," in *OCEANS 91 Proceedings*, vol. 1, pp. 254–260, Oct 1991.

[13] G. R. Mackelburg, "Acoustic data links for uuvs," in *OCEANS 91 Proceedings*, pp. 1400–1406, Oct 1991.

[14] K. F. Scussel, J. A. Rice, and S. Merriam, "A new mfsk acoustic modem for operation in adverse underwater channels," in *OCEANS '97. MTS/IEEE Conference Proceedings*, vol. 1, pp. 247–254 vol.1, Oct 1997.

[15] L. Freitag, M. Stojanovic, S. Singh, and M. Johnson, "Analysis of channel effects on direct-sequence and frequency-hopped spread-spectrum acoustic communication," *IEEE Journal of Oceanic Engineering*, vol. 26, pp. 586 – 593, 11 2001.

[16] E. Demirors and T. Melodia, "Chirp-based lpd/lpi underwater acoustic communications with code-time-frequency multidimensional spreading," in *Proceedings of the 11th ACM International Conference on Underwater Networks & Systems*, WUWNet '16, (New York, NY, USA), pp. 9:1–9:6, ACM, 2016.

[17] X. ling Cao, W. hua Jiang, and F. Tong, "Time reversal mfsk acoustic communication in underwater channel with large multipath spread," *Ocean Engineering*, vol. 152, pp. 203 – 209, 2018.

[18] J. Proakis, *Digital Communications*. McGraw-Hill series in electrical and computer engineering : communications and signal processing, McGraw-Hill, 2001.

[19] M. Stojanovic, J. Proakis, J. Rice, and M. Green, "Spread spectrum underwater acoustic telemetry," *OCEANS '98 Conference Proceedings*, pp. 650 – 654 vol.2, 01 1998.

[20] E. M. Sozer, J. G. Proakis, R. Stojanovic, J. A. Rice, A. Benson, and M. Hatch, "Direct sequence spread spectrum based modem for under water acoustic communication and channel measurements," in *OCEANS '99 MTS/IEEE.*, vol. 1, pp. 228–233 vol.1, 1999.

[21] B. Vucetic and J. Yuan, *Turbo Codes: Principles and Applications*. Kluwer Academic Publishers, 2000.

[22] A. Dobbin and J.-F. Bousquet, "Reliable acoustic link using non-coherent turbo-coded frequency shift keying," *WUWNET '17, November 6-8, 2017, Halifax, Canada*, pp. 1–2, 11 2017.

[23] J. Potter, J. Alves, D. Green, G. Zappa, I. Nissen, and K. McCoy, "The JANUS underwater communications standard," *2014 Underwater Communications and Networking (UComms)*, pp. 1–4, Sept 2014.

[24] G. Ferri*, A. Munafò*, A. Tesei, P. Braca, F. Meyer, K. Pelekanakis, R. Petroccia, J. Alves, C. Strode, and K. LePage, "Cooperative robotic networks for underwater surveillance: an overview," *IET Radar, Sonar Navigation*, vol. 11, no. 12, pp. 1740–1761, 2017.

[25] M. Stojanovic and J. Preisig, "Underwater acoustic communication channels: Propagation models and statistical characterization," *IEEE Communications Magazine*, vol. 47, pp. 84–89, January 2009.

[26] J. Alves, T. Furfaro, K. LePage, A. Munafò, K. Pelekanakis, R. Petroccia, and G. Zappa, "Moving janus forward: A look into the future of underwater communications interoperability," in *OCEANS 2016 MTS/IEEE Monterey*, pp. 1–6, Sept 2016.

[27] A. Viterbi, "Convolutional codes and their performance in communication systems," *IEEE Transactions on Communication Technology*, vol. 19, pp. 751–772, October 1971.

Appendix A: Personnel at Sea

- Jean-François Bousquet (Scientist-in-Charge as well as communications system lead)
- Paul Hines (Acoustician/Sea-Trial Specialist)
- David Barclay (Physical Oceanographer)
- Maxime Miron-Morin (Receiver Deployment)
- Andrew Dobbin (Signal processing, Transmitter)
- Richard Cheel (Marine Operations)
- Greg Trowse (Marine Operations)
- Carmen Goodwin (Ship Captain)

Appendix B: Equipment Checklist during Final Trials

- Transmitter System
  - Acoustic projector
  - QSC PL380 Audio Power Amplifier, sold by RaveAV.
  - Audio transformer box
  - Extension cable for power supply
  - Audio cables with converter
  - High power cables to connect to/from transformer box
  - 110-V 2000-W Power Generator (Luna Ocean)
  - UPS
  - Panasonic Toughbook with required software (Audacity, Matlab, TRAC)
  - Signal cable to extend the projector depth
  - 1 15-kg weights for the transmitter
  - 1 40-meter 3-strand Dyneema cable
  - 2 Multimeters
- VLA
  - TR-ORCA with replenished batteries
  - Collar float
  - Hydrophone vertical linear array
  - Acoustic release

  - Acoustic links
  - 40-meter 3-strand Dyneema cable
  - 5 meter nylon between anchor and acoustic release.
  - Twine to attach acoustic link.
  - 200-lbs weight (Luna)
  - End connectors to seal the case
  - Eye bolts
  - 2 synthetic buoys
  - Reconfiguration cable
  - All end caps
- Monitoring system
  - TR-ORCA-MINI with replenished batteries
  - TR-float with RF antenna
  - TR-float basestation
  - Omni antenna
  - Cantenna
  - 2 15-meter ethernet cables (green)
  - Asus laptop to reconfigure receivers.
  - Ethernet to USB converter.
  - USB stick (Andrew)
  - Monitoring hydrophone
  - 1 5-kg weights for the monitoring buoy

  - Mooring system (Luna)
  - 2 synthetic buoys

- Support & Monitoring Equipment
  - Radios or cellphones
  - Handheld GPS unit(s).
  - Hand deployable CTD (CastAway)
  - ADCP (or LIDAR) (Oceanography Dept.)
  - Ultra sonic ranger (Oceanography Dept.)
  - 2 depth loggers for transmitter and VLA.
  - Tape measure
  - Scissors
  - Knife
  - Tie wraps